Nuclear scaling is coordinated among individual nuclei in multinucleated muscle fibers.

Stefanie E. Windner[1], Angelika Manhart[2], Amelia Brown[1], Alex Mogilner[2], Mary K. Baylies[1*]

[1] Developmental Biology Program, Sloan Kettering Institute, New York, NY 10065
[2] Courant Institute, New York University, New York, NY 10012

[*] Corresponding author (m-baylies@ski.mskcc.org)

Key words
Nuclear Scaling, Cell Size, Skeletal Muscle, Nuclear Coordination, Nuclear Compensation, Nuclear synthetic activity, Nuclear positioning, Syncytial organization, Polyploidy, Drosophila

SUMMARY

Optimal cell performance depends on cell size and the appropriate relative size, i.e. scaling, of the nucleus. How nuclear scaling is regulated and contributes to cell function is poorly understood, especially in skeletal muscle fibers, which are among the largest cells, containing hundreds of nuclei. Here we present a *Drosophila in vivo* system to analyze nuclear scaling in whole multinucleated muscle fibers, genetically manipulate individual components, and assess muscle function. Despite precise global coordination, we find that individual nuclei within a myofiber establish different local scaling relationships by adjusting their size and synthetic activity in correlation with positional/spatial cues. While myonuclei exhibit compensatory potential, even minor changes in global nuclear size scaling correlate with reduced muscle function. Our study provides the first comprehensive approach to unraveling the intrinsic regulation of size in multinucleated muscle fibers. These insights to muscle cell biology will accelerate the development of interventions for muscle diseases.

Highlights

- Muscle nuclei collectively establish precise global scaling with muscle fiber size
- Cells contain domains with distinct local scaling of DNA, nuclear and nucleolar sizes
- Nucleolar scaling indicates proportionally higher synthetic activity in small nuclei
- Changes in DNA content affect nuclear scaling relationships and muscle function

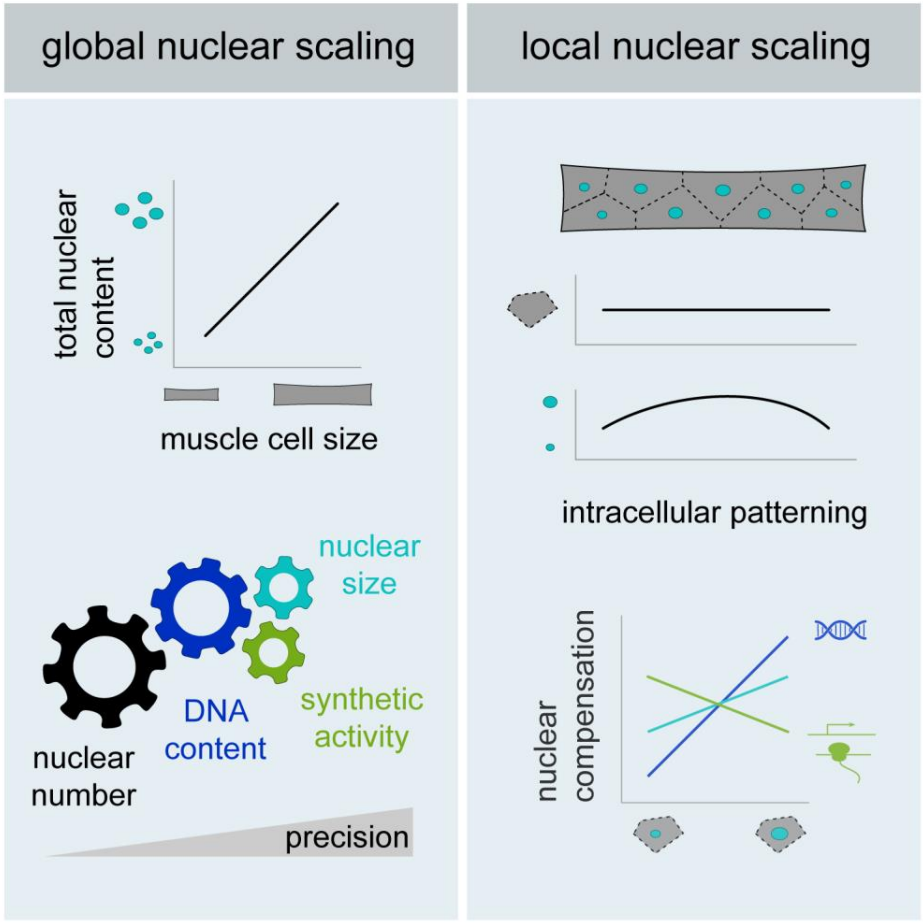

INTRODUCTION

The physical dimensions of a cell and the appropriate relative size of its organelles are essential for cell structure and function. Cell size and intracellular scaling relationships are established and actively maintained in a cell type-specific manner by integrating both extrinsic and intrinsic signals. Extrinsic size regulation includes systemic factors like nutrition, Insulin signaling, and hormones, which determine organ and overall body size by regulating cell numbers and sizes (Boulan et al., 2015; Penzo-Méndez and Stanger, 2015). Intrinsically, individual cells continuously assess their size in relation to their target size and adjust their growth and synthetic activity rates to optimize cell function (Amodeo and Skotheim, 2016; Chan and Marshall, 2012; Ginzberg et al., 2015). While the molecular mechanisms of systemic cell size regulation are rather well-characterized, less is known about the intrinsic side.

Intrinsic regulators of cell size include DNA content, nuclear size, and nuclear activity (Frawley and Orr-Weaver, 2015; Miettinen et al., 2014; Mukherjee et al., 2016). The amount of nuclear DNA shows a coarse correlation with cell size (e.g. diploid cardiomyocytes are smaller than polyploid ones); however, different diploid cell types within the same organism establish a wide variety of cell and nuclear sizes (Gillooly et al., 2015). In contrast, each cell type can be characterized by a specific ratio of nuclear to cytoplasmic volume (nuclear size scaling) (Conklin, 1912). The precise regulation of nuclear size affects DNA organization, transcriptional and translational processes, nuclear import and export, and transport/diffusion of products throughout the cytoplasm (Levy and Heald, 2012). Further, nuclear size scaling determines the concentration of nucleolar components inside the nucleus, which regulates the size of the nucleolus (Weber and Brangwynne, 2015). Nucleolar size closely correlates with Pol I transcription activity and ribosome biogenesis, and plays a crucial role in cell growth and size control (Brangwynne, 2013; Neumüller et al., 2013; Rudra and Warner, 2004). Studies using a variety of systems have indicated that size regulation of the nucleolus via nuclear size scaling could represent a crucial mechanism that couples cell size with nuclear synthesis and growth rates (Eaton et al., 2011; Ma et al., 2016). Thus, changes in nuclear and nucleolar size scaling provide information about the cell state, especially its synthetic activities and the metabolic demands of the cell. While nuclear and nucleolar sizes are routinely used as diagnostic indicator for a variety of disease states (Jevtić

and Levy, 2014), the mechanisms that coordinate different cellular components and activities to establish and maintain specific cell sizes remain largely elusive.

Skeletal muscle fibers are one of the largest cell types and possess remarkable cell size plasticity. Individual cells develop and grow by fusion of myoblasts and can contain hundreds of nuclei distributed across the cell surface (Deng et al., 2017). Based on the limited synthetic capacity of a single nucleus and the physical limitations to cellular transport and diffusion, a longstanding hypothesis (known as myonuclear domain hypothesis) postulates that, each nucleus in a muscle syncytium only supplies its immediately surrounding cytoplasm with gene products (Hall and Ralston, 1989; Pavlath et al., 1989). Accordingly, studies using different model systems have suggested that muscle nuclei are positioned to minimize transport distances throughout the cytoplasm (Bruusgaard et al., 2003; Manhart et al., 2018). Across species, the number of myonuclei is considered the main determinant of overall muscle cell size, however, nuclear numbers vary depending on factors like muscle fiber type, activity, or age, indicating that the average size of the cytoplasmic domain associated with each nucleus is highly variable (Van der Meer et al., 2011). Further, differences exist within a muscle fiber in nuclear density and/or gene expression, particularly in nuclei adjacent to specialized sub-cellular structures like muscle attachment sites (myotendinous junctions, MTJs) and the motoneuron synapse (neuromuscular junction, NMJ) (Bruusgaard et al., 2003; B. Rosser and Bandman, 2003). While this suggests that muscle nuclei can adjust their synthetic activity dependent on cell size and functional demands (K. Gundersen, 2016; Murach et al., 2018a), it is still not clear how the contribution of individual nuclei to cell size is coordinated in a shared cytoplasmic space and whether nuclear size scaling plays a role in regulating muscle fiber size.

Diseases of the skeletal musculature are commonly associated with changes in nuclear positioning, nuclear sizes, and nuclear activities (Folker and Baylies, 2013; Malfatti and Romero, 2017; Schreiber and Kennedy, 2013), but how different muscle phenotypes result in reduced muscle function remains poorly understood. The size and the complexity of muscle tissue in vertebrates impose technical challenges that limit studies on fiber size and intracellular organization to tissue cross-sections or *in vitro* approaches. To provide a more comprehensive understanding of nuclear scaling relationships and the intrinsic regulation of cell size in multinucleated muscle fibers, we have developed a *Drosophila in vivo* system to quantify cell and nuclear parameters in fully differentiated muscle cells, genetically manipulate individual cellular

components, and evaluate muscle function. This system allowed us to analyze nuclear scaling relationships on a global level (scaling of the cumulative nuclear content with total cell size) and a local level (scaling of individual nuclei with their surrounding cytoplasmic domain) and identify possible mechanisms of nuclear coordination and compensation within individual muscle fibers.

RESULTS

Drosophila larval body wall muscles allow for 2D quantification of cell and nuclear sizes

The body wall musculature of the *Drosophila* larva is a well-established system to investigate fundamental aspects of muscle cell biology *in vivo* (Demontis et al., 2013; Deng et al., 2017; Keshishian et al., 2003; Piccirillo et al., 2014). The musculature is comprised of 30 different muscles, which are arranged in the same stereotyped pattern in every abdominal hemisegment (Schulman et al., 2015). Each of these glycolytic muscles consists of only one multinucleated cell with distinct size, shape, and attachment sites, and is easily accessible in live or dissected preparations (Dobi et al., 2015). Here we focused on two muscles, Ventral Longitudinal muscles VL3 and VL4 (also known as muscles 6 and 7), which are flat rectangular cells with disc-shaped nuclei located on only one cell surface (Figures 1A and 1B). We compared 2D and 3D quantification of cell and nuclear sizes and found that volumes and areas are proportional due to the minimal and very consistent depth of VL muscle cells and nuclei. (Figures 1C-E and S1A-B). Thus, this system allows for accurate quantification of the size of whole muscle cells and their nuclei on z-projections of confocal stacks.

To assess the full range of VL muscle sizes at the end of larval development, we used carefully staged third instar larvae from three genetic control backgrounds (see Methods) and quantified VL3 and VL4 muscles at different positions along the anterior-posterior axis of each larva (abdominal hemisegments 2-6). On average, VL3 muscles were 65% bigger than VL4 muscles, with comparable sizes across individual larvae and genotypes (mean VL3: 39767 μm^2, 15 nuclei; mean VL4: 25633 μm^2, 10 nuclei; Figures 1F and 1G). Within each larva, VL3 muscles were significantly bigger in the anterior hemisegments 2-4 and approximated the size of VL4 muscles in more posterior hemisegments (Figure 1H and 1I). In contrast, VL4 muscle size was consistent along the anterior-posterior axis of the larvae (Figure 1H). In both VL muscles, the average number of nuclei per cell decreased from anterior to posterior (Figure S1C). Together,

VL3 and VL4 muscles provided a significantly different, but overlapping, range of cell sizes and nuclear numbers.

To further validate our dataset, we performed unsupervised cluster analysis using the following parameters: cell area, cell shape (aspect ratio: length/width), cell position (abdominal hemisegment number), number of nuclei, and cumulative nuclear area. Clustering divided the data into two groups that did not show any bias for individual larvae, genotypes, or experimental replicates (Figure S1D), but clearly correspond to VL3 and VL4 muscles (Figure 1J). These analyses confirmed that, VL3 and VL4 muscles were comparable across larvae and genotypes, but inherently different when compared to each other.

Muscle nuclei collectively establish precise global scaling with cell size

To achieve a comprehensive characterization of nuclear scaling with regard to the size of multinucleated muscle fibers (*global* nuclear scaling), we took advantage of the natural variation of cell size parameters that we observed in wild-type VL muscles. In addition to cell areas and nuclear numbers, we quantified the cumulative nuclear DNA content (ploidy), the cumulative area of all nuclei, and the cumulative area of all nucleoli within each cell (Figures 2A-2C). All parameters showed linear scaling with cell size across VL muscle types, however, with different linear fits (Figures 2D-2G). During *Drosophila* development, fusion of diploid embryonic myoblasts initially sets the number of nuclei per muscle fiber. Subsequently endoreplication increases the DNA content within each nucleus to promote muscle growth in the larva (Demontis and Perrimon, 2009). Nuclear numbers ranged from 9-21 in VL3 and from 6-13 in VL4, with a considerable variation in cell sizes for every given number of nuclei (Figure 2D, correlation coefficient R=0.74). We independently assessed the DNA content in VL muscles by calculating ploidy numbers in muscle nuclei based on Hoechst fluorescence intensities in diploid muscle progenitor cells (AMPs, Figures 2B and S2A-F). On average, VL3 muscles contained a total of 614+/-153 copies, VL4 muscles a total of 386+/-96 copies of DNA. Notably, cells with the same number of nuclei contained different amounts of cumulative DNA content, resulting in improved linear scaling with cell area (Figure 2E, R=0.86). Compared to DNA content, the cumulative area of all nucleoli and nuclei showed further improved scaling with VL cell size (Figures 2F and 2G; R=0.88 and R= 0.90, respectively). Plotted on a log scale, cumulative nucleolar, cumulative nuclear and cell areas showed a linear scaling relationship (Figure S2G). Similar to DNA content,

cells with the same number of nuclei established widely different cumulative nucleolar and nuclear sizes. These data showed that VL muscle fibers establish precise global nuclear scaling relationships despite variations in the number of their nuclei. Further, this suggested a high level of coordination among the nuclei contained within a cell.

To directly compare muscle fibers with varying nuclear numbers and analyze the relationships between DNA content and nuclear and nucleolar sizes, we normalized all global parameters by the number of nuclei per cell. Thereby we calculated the average size of the cytoplasmic domain per nucleus (cell area/nuclear number), the average DNA content per nucleus (cumulative DNA content/nuclear number), and the average size of nuclei and nucleoli (cumulative area/nuclear number). Average cytoplasmic domain sizes showed a similar distributions and range in VL3 and VL4 muscles (Figure 2H), suggesting a similar optimal cytoplasmic domain size (~ 3000 μm^2) per nucleus in both VL muscles. In muscles with near-optimal cytoplasmic domain sizes, average DNA content (46c), average nuclear areas (187 μm^2), and average nucleolar areas (41μm^2) were similar. These parameters were reduced by ~20-30% in cells with smaller domain sizes and increased by ~20-30% in cells with larger domain sizes (Figure 2I). As muscle cells grow by adding DNA content, this stepwise growth pattern could reflect a stepwise increase in nuclear DNA via endoreplication.

To further investigate size scaling of nuclei and nucleoli, we determined the ratio of cumulative nuclear area per cell area (global nuclear size scaling) and the ratio of cumulative nucleolar per nuclear area (global nucleolar size scaling) (Figure 2J). On average, VL3 and VL4 muscles established significantly different global nuclear size scaling relationships, while global scaling of nucleoli to nuclei was similar in both muscles (Figures S2H and S2I). Given the function of the nucleolus in ribosome biogenesis and cell growth, proportionally larger nuclei and nucleoli in VL3 muscles indicated overall higher metabolic potential per nucleus. Strikingly, in both VL muscles, the relationship between nuclear and nucleolar scaling changed with absolute size, so that cells with near-optimal cytoplasmic domain sizes contained proportionally large nuclei and small nucleoli, while cells with smaller or larger cytoplasmic domain sizes contained proportionally small nuclei and large nucleoli (Figure 2K and S2J). This further indicated that muscle cells globally coordinate nuclear and nucleolar scaling to adjust nuclear synthetic activities dependent on DNA content and the average size of the cytoplasmic domains.

Together these data demonstrated that a variety of nuclear parameters scale with the size

of multinucleated muscle fibers; however, similar to mononucleated/diploid cells, the cumulative size of all nuclei and nucleoli give the best prediction of muscle cell size. We propose that global nuclear scaling with VL muscle size is achieved in three steps: firstly, the number of nuclei sets a range of possible cell sizes; secondly, each cell during growth individually increases nuclear ploidies to maintain a stable scaling of cumulative of DNA content with cell size. Thirdly, the size of nuclei and nucleoli is continuously adjusted, to establish precise, cell type specific scaling with cell size, and allow for optimal cell function.

Nuclei distribute via a force balance and adjust their size based on spatial cues

The accuracy of global nuclear scaling in multinucleated VL muscles suggested that the nuclei contained within a cell are highly coordinated. We hypothesized that stable global scaling relationships are established via scaling of individual nuclei with their surrounding cytoplasmic domain (*local* nuclear scaling). To test this, we determined nuclear positions within each cell based on their centroids, and thus independent of their size (Figure 3A). In both VL muscles, the distances between nuclei (Nearest Neighbor Distances) were larger than expected for random distribution, confirming that nuclei are deliberately positioned (Figure S3A). Along the length of each fiber, nuclei were organized in rows, typically two rows in VL3 and one row in VL4 muscles (Figure 3B). However, in VL3 and VL4 muscles with the same geometric properties (cell dimensions, number of nuclei) the number and the position of rows were similar (Figure 3C), indicating that geometrical factors, rather than VL muscle type, dictate the nuclear patterns.

In *Drosophila* and mammalian muscle fibers, nuclear positioning involves microtubules and motor proteins to generate mechanical forces (Folker and Baylies, 2013; G. G. Gundersen and Worman, 2013; Roman and Gomes, 2017). In larval VL3 and VL4 muscles, microtubules grow from the nuclear envelopes and form astral arrays surrounding each nucleus (Figure S3B) (Metzger et al., 2012; Volk, 2013; Rosen et al. in press). We hypothesized that these microtubule asters interact with each other and with the cell edges, potentially through microtubule-associated motors, and that these mechanical interactions position the nuclei (Figure 3D). We performed mathematical simulations to test whether such mechanical forces were sufficient to explain the nuclear positioning in VL3 and VL4 muscles (see Methods). In brief, we assumed that the nuclei interact with each other and with the cell edges via pair-wise, distance dependent forces. We assumed that these forces are repulsive and decrease with distance. We also tested differences in

the relative magnitude of inter-nuclear and nucleus-cell edge forces but kept the forces independent of nuclear sizes and positions. For each experimentally measured cell, we used the real cell dimensions and nuclear numbers, and initially placed the nuclei at their measured positions. Then, applying the distance-dependent forces, we calculated their resulting positions caused by force balancing (Figure 3D). The simulated data, shown in Figures 3B and 3C, closely recapitulated the experimentally measured nuclear positioning in both VL3 and VL4 cells. The accuracy of the mathematical approximation supported that positioning mechanisms are based on microtubule-based mechanical forces and establish a cell geometry-dependent force balance to position the nuclei in VL3 and VL4 muscles.

If nuclei are positioned via mechanical interactions yet independent of their size, we hypothesized that these nuclei sense the size of their surrounding cytoplasmic domain and adjust their own size accordingly, to establish local size scaling relationships. To evaluate this hypothesis, we tested a space-sensing mechanism that predicts the size of each nucleus based on the detected amount of a hypothetical diffusible cytoplasmic molecule (Figure 3E). We assumed that signal molecules are activated or created with a constant rate and equal probability everywhere in the cell, diffuse and, upon encountering a nucleus, are taken up by the nucleus. Subsequently, each nucleus adjusts its size depending on how much signal it receives (see Methods and Mathematical Supplemental Methods). Using experimentally determined cell shapes and nuclear positions, our simulations predicted nuclear areas very accurately, with an average relative error of less than 17% compared to the experimental data (Figure 2F). An intuitive explanation for this mechanism is that nuclei positioned farther away from their neighbors harvest the signaling molecules from the greater area, and hence grow larger than their neighbors, leading to the local size regulation. Our data suggest that a local space sensing mechanism is involved in regulating nuclear sizes within each cell.

Our space-sensing model predicted correlations between the size of individual nuclei and the size of their surrounding cytoplasmic domain. To test this *in vivo*, we used an unbiased approach to geometrically partition each cell into cytoplasmic domains based on nuclear positions (Voronoi tessellation (Du et al., 2010), Figure 3A). In accordance with our simulations, we found a linear correlation between nuclear and Voronoi areas in both VL muscle types (Figure 3G). However, in contrast to the precise global nuclear size scaling relationships (Figure 2G, R=0.90), the local correlation of nuclear size and cytoplasmic domain size was much weaker (R=0.55).

Closer analysis revealed that Voronoi domain areas were relatively consistent within each muscle fibers (Figure 3H), while the size of individual nuclei varied significantly (Figures 3I). Strikingly, in both VL muscles, nuclear areas showed a specific, asymmetric pattern with the biggest nuclei located close to the cell center and considerably smaller nuclei at the cell ends. This intracellular pattern of nuclear sizes was not predicted by our space-sensing model (Figure S3C), indicating that additional *regional* factors differentially affect nuclear sizes along the length of each VL muscle fiber. Multiple linear regression analyses using various cell parameters confirmed that the best prediction of nuclear size was achieved by a combination of local cytoplasmic domain area and nuclear position within the cell (Figure 3J, $R=0.66$, $p<0.0001$). This demonstrated that VL muscle nuclei do establish specific local size scaling with their surrounding cytoplasmic domain; however, each cell contained a heterogeneous population of nuclei with different sizes.

Together these data suggested that VL nuclei are coordinated, via a force balance, to evenly distribute throughout the cells and establish stable global scaling relationships by adjusting their size based on local spatial parameters. In addition to the size of the cytoplasmic domain, our data predicts that regional factors, which consistently vary along the length of each muscle fiber, regulate nuclear sizes within each VL muscle.

Muscle fibers are composed of domains with distinct nuclear scaling relationships

Each skeletal muscle fiber attaches to tendon cells at both cell ends (myotendinous junctions, MTJs) and is innervated by a motoneuron at the neuromuscular junction (NMJ). VL3 and VL4 muscles form MTJs at the anterior and posterior abdominal hemisegment boundaries and are innervated by the same motoneuron off-center, in the anterior half of the cells (Figure 4A). Strikingly, in both VL muscles, the highest local nuclear size scaling values (Nuclear area / Voronoi area) correlated with the position of the NMJ (start: 29+/-5%, end: 54+/-8% of cell length), while nuclei adjacent to anterior and posterior MTJs showed significantly lower values (Figures 4B and S4A). This indicated that, within each VL muscle fiber, differences in nuclear size scaling correlate with regions associated with specific cell functions during muscle contraction.

To determine whether nuclear DNA content affects local nuclear size scaling, we calculated DNA copy numbers for each VL nucleus, using established techniques (e.g. Losick et al., 2013). We identified nuclei with 16, 32, or 64 copies of DNA, which on average, occurred at a similar

frequency in VL3 and VL4 muscles (Figures 4C-E and S2A-D). However, each cell established a distinct ratio of nuclear ploidy numbers in correlation with the number of nuclei and cell size, so that cells with larger cytoplasmic domain sizes contained a higher percentage of 64c nuclei. Along the cells, 16c nuclei were located adjacent to the MTJs and were absent from the NMJ region; 32c nuclei were positioned throughout the cell, and 64c nuclei were located mainly adjacent to the NMJ (Figure 4F). On average, nuclear DNA content was highest in nuclei adjacent to the NMJ in both VL muscles (Figure S4B). We compared size parameters associated with 32c and 64c nuclei: a doubling in DNA content correlated with significant increases in nuclear area (~35%) and cytoplasmic (Voronoi) domain area (~21%). Further, local nuclear size scaling (nuclear area/Voronoi area) was increased for 64c nuclei (Figure 4G). These data suggested that nuclear ploidy affects absolute size, as well as local nuclear size scaling. Nevertheless, both 32c and 64c nuclei established similar size scaling patterns along the anterior-posterior axis of the VL muscle fibers (Figure 4H), indicating that regional/intracellular size scaling differences are established independent of absolute nuclear DNA content.

Variations in nuclear DNA content suggested significant local differences in nuclear synthetic activity within each VL muscle fiber. We analyzed individual nucleolar sizes as readout for the synthetic activity of VL muscle nuclei (Figure 4I). Across all VL nuclei, absolute nucleolar areas showed a better linear correlation with nuclear areas than with Voronoi domain areas and were significantly larger in 64c than in 32c nuclei (~24%; Figures 4G and S4C-D). Accordingly, mean nucleolar areas were largest in the anterior half of the muscle fibers and the NMJ region (Figure 4J). To independently assess nuclear synthetic activity, we analyzed labeling of H3K9ac, a conserved marker of gene activation which does not report rRNA transcription (Boros, 2012; Peng and Karpen, 2007). H3K9ac fluorescence intensities indicated that the mean number of active transcriptional start sites increased proportional with nuclear ploidy; thus, normalizing by DNA content resulted in similar relative H3K9ac levels in 16c, 32c and 64c nuclei (Figure 4K). Along the length of both VL muscles, H3K9ac levels showed clear regional differences and were proportionally increased in the anterior half of the cells (Figure 4L). Together, DNA content, nucleolar sizes, and H3K9ac indicated highest nuclear activity in the anterior half of the cells, including the region of the NMJ.

We used the local scaling of nucleolar to nuclear areas to further investigate the relative contribution of individual nuclei to the total synthetic activity of each cell. In mononucleated cells

with a set number of nucleolar components, nucleolar size is determined in a concentration-dependent manner by the relative size of the nucleus within the cell (Brangwynne, 2013; Ma et al., 2016; Uppaluri et al., 2016; Weber and Brangwynne, 2015). If muscle nuclei contribute to a shared pool of nucleolar components, small nuclei containing less DNA would import a proportionally increased number of nucleolar components and form proportionally larger nucleoli. Indeed, local nucleolar size scaling was significantly increased in 32c nuclei, indicating proportionally higher nuclear synthetic activity in nuclei containing less DNA (Figure 4G). Along the anterior-posterior axis of the cells, the pattern of nucleolar size scaling showed specific regional differences that were recapitulated by both 32c and 64c nuclei, and similar in VL 3 and VL4 muscles (Figures 4M). These results indicated that nucleolar size scaling (nucleolar area/nuclear area) was established independent of absolute size parameters. Intriguingly, the intracellular pattern of nucleolar size scaling was inverted compared to nuclear size scaling, so that nucleolar size scaling was lower in proportionally large nuclei and higher in proportionally small nuclei (Figure 4N). These data suggested that within each muscle cell, size scaling of nucleoli could coordinate nuclear synthetic activities to compensate for differences in nuclear DNA content as well as for differences in local nuclear size scaling.

Together these data showed that each muscle fiber consist of domains with distinct nuclear scaling relationships. Scaling of nuclear size, DNA content, and synthetic activity exhibit different, asymmetric patterns along the length of both VL muscle fibers, and correlate with regions associated with different cell functions during muscle contraction. We propose inverse size scaling of the nucleolus as a possible mechanism for muscle cells to allow for local differences in DNA content and nuclear sizes, while maintaining similar cytoplasmic domain sizes along each muscle fiber and stable global cell size regulation.

Nuclear compensation and functional consequences

Our analyses suggested that DNA content affects the absolute size of cells, nuclei, and nucleoli, while nuclear positioning and local size scaling are regulated independent of nuclear ploidy. To test our assumptions and investigate the robustness of nuclear scaling and cell function, we genetically manipulated the DNA content in the larval musculature. We knocked down a component of the DNA replication machinery (Dmef2 > ctd1(dup)RNAi) to reduce the amount of endoreplication (Whittaker et al., 2000), and overexpressed a regulator of cell cycle progression

(Dmef2 > dMyc) to promote endoreplication specifically in muscle during larval growth (Pierce et al., 2004). These manipulations resulted in significant differences in nuclear DNA content: Cdt(Dup) knockdown (KD) reduced nuclear ploidy numbers by one round of endoreplication (8c, 3%; 16c, 83%; 32c, 14%), whereas Myc overexpression (OE) increased nuclear ploidies by approximately one round of endoreplication (32c, 6%; 64c, 38%; 128c, 55%; 256c, 1%) (Figures 5A and S5A). Cdt1(Dup)KD muscles were only 10% smaller, and MycOE muscles had similar cell sizes compared to controls; however, larval locomotion was significantly reduced in both genotypes (Figures 5B and S5B). This indicated that our tissue specific manipulations of DNA content negatively affected muscle function but did not override the systemic demands for a specific muscle size. These manipulations thus provided an opportunity to investigate nuclear adaptions to changes in intracellular scaling relationships.

Analysis of global nuclear scaling relationships (cumulative nuclear parameter/cell size) showed that Cdt1(Dup)KD and MycOE did not affect the number of VL nuclei, thus scaling of nuclear number with cell size was similar to control muscles (Figures 5C and S5C). Despite changes in absolute parameter values, precise linear scaling of cumulative DNA content and nuclear and nucleolar areas with VL cell areas was also maintained in Cdt1(Dup)KD and MycOE backgrounds (Figures 5D-5F). These data indicated that intracellular scaling mechanisms and the coordination of nuclei within each cell were not disrupted and were independent of absolute size parameters. In accordance with our simulations of nuclear positioning in control cells, Cdt1(Dup)KD and MycOE nuclei were evenly positioned despite different nuclear sizes and DNA content (Figures S5D and S5E). Further, in both genotypes, DNA ploidy numbers and nuclear sizes were smallest adjacent to the MTJs and increased towards the cell center/NMJ (Figures S5F and S5G). Strikingly, the normalized distribution of nuclear sizes along each cell was similar in MycOE, Cdt1(Dup)KD, and control muscles (Figure 5G), suggesting that regional patterning mechanisms within the cell were intact and regulate relative sizes rather than absolute nuclear parameters within each cell.

On average, Cdt1(Dup)KD resulted in a 62% reduction in total DNA content, and 60% reduction in cumulative nucleolar areas, while the cumulative area of all nuclei was only 25% smaller than in control cells (Figures S5H-J). Thus, Cdt1(Dup)KD nuclei increased their size relative to DNA content. However small nucleolar sizes suggested that synthetic activity was not upregulated under these conditions (e.g. no compensation). Instead, cumulative nucleolar areas

maintained a linear correlation with total DNA content (Figure 5H), suggesting that the amount of nuclear DNA limits maximal nucleolar sizes within each muscle cell. In accordance with a low number of nucleolar components and proportionally increased nuclear sizes, nucleolar size scaling (nucleolar size/nuclear size) was significantly decreased in Cdt1(Dup)KD nuclei compared to control (Figure 5I). Despite lower global size scaling values in Cdt1(Dup)KD muscles, the regional patterns of local nuclear and nucleolar size scaling within the cells were similar to control (Figure 5K). These data indicated that local size scaling mechanisms were intact in Cdt1(Dup)KD muscles. Limitations to the synthetic machinery could reduce muscle function and growth by not meeting the metabolic demands of the muscle cells.

In contrast to Cdt1(Dup)KD, MycOE resulted in a doubling in cumulative DNA content, a four-fold increase in cumulative nucleolar area, and a doubling in cumulative nuclear area (Figures S5H-J). In addition to promoting the replication of nuclear DNA, MycOE has been shown to promote rRNA synthesis, ribosome biogenesis, and nucleolar sizes in a variety of *Drosophila* larval tissues (Grewal et al., 2005). Despite the dramatic increase in nucleolar areas, MycOE muscle nuclei maintained linear scaling of cumulative DNA content with cumulative nuclear areas similar to control cells (Figure 5J). This suggested that the ratio of DNA per nuclear area, and thus chromatin compaction and mechanical properties of the nucleus, might limit the range of nuclear size adjustments in dynamically contracting muscle fibers. In accordance with increased absolute sizes, local size scaling of nuclei and nucleoli was dramatically increased in (Figure 5I). Further, along the anterior-posterior length of MycOE muscles, the coordination between local nuclear and nucleolar size scaling was lost (Figure 5L), suggesting that the upregulation of the synthetic machinery in Myc OE disrupted local size sensing mechanisms.

Together these data suggest that VL muscle nuclei regulate their size within a range set by DNA content, yet differentially respond to increases and decreases in nuclear ploidy. While DNA content affects absolute nuclear sizes and synthetic activity, nuclear positioning mechanisms and functionally distinct regions within each cell determine the relative contribution of individual nuclei to cell size. These experiments highlight distinct levels of muscle size regulation in multinucleate muscle fiber (Figure 6), demonstrate the robustness of intracellular organization, and stress the importance of nuclear scaling for muscle function.

DISCUSSION

Skeletal muscle fibers are large multinucleated cells with essential roles in locomotion and metabolism. Our study provides the first comprehensive analysis of nuclear scaling in whole, fully differentiated muscle fibers using a large *in vivo* dataset. We show that muscle nuclei collectively establish precise global scaling relationships with muscle cell size. However, each cell is composed of domains with distinct local scaling of DNA, nuclear size, and nuclear synthetic activities. Together, our analyses of wild-type parameters, mathematical simulations, and genetic manipulations reveal different levels of muscle size regulation (Figure 6) and implicate nuclear scaling as essential for muscle function. We suggest that the mechanisms involved in intracellular size regulation in muscle cells depend on local factors (cytoplasmic domain size), regional factors (possibly involving NMJ, MTJs), as well as global factors (muscle type).

To establish a baseline for nuclear scaling in multinucleated muscle fibers we took advantage of the natural variation of different size parameters in *Drosophila* VL muscles. In *Drosophila* as well as in vertebrate systems, muscle fibers exhibit remarkable size plasticity, and nuclear number and DNA content are highly variable (Deng et al., 2017; Van der Meer et al., 2011). VL muscle sizes vary along the anterior-posterior axis of each larva and correlate with a specific range in the number of nuclei. We find that, on the global level, several nuclear parameters scale with muscle cell size, including nuclear number, DNA content, nucleolar size, and nuclear size. While the correlation of nuclear number and DNA content with muscle cell size has been appreciated in a variety of systems, nuclear size scaling has not been previously investigated in muscle fibers. Our data indicate that DNA content establishes a coarse scaling with cell size while the size regulation of nuclei and nucleoli is used for fine tuning the system. The precision of global nuclear and nucleolar size scaling in VL muscles is reminiscent of mononucleated cells, where cell-type specific scaling of the nucleus and nucleolus are associated with optimal cell function (Levy and Heald, 2012). Strikingly, VL3 and VL4 muscles establish distinct global nuclear size scaling, indicating that intracellular size scaling relationships are established in a muscle type specific manner. While the metabolic consequences of global size scaling differences in wild-type *Drosophila* muscles remain to be determined, it is possible that scaling of nuclear and nucleolar sizes with cell size is indicative of the growth potential of individual cells, and the differences in functional demands observed in different vertebrate muscle fiber types.

Despite precise global scaling, the nuclei contained within each VL muscle fiber

consistently differ in size, DNA content, and nucleolar size. These differences are established in particular patterns along the length of both VL muscles and are independent of absolute cell size and nuclear content. While regional nuclear differences have been reported in different vertebrate muscles (Bruusgaard et al., 2003; B. W. C. Rosser et al., 2002), the extent of nuclear diversity and the precision of nuclear patterning within individual fibers and on population level have not been documented. In both *Drosophila* and vertebrate muscles, increases in DNA content are associated with the position of the NMJ. While in vertebrate muscles this seems to be achieved by regional clustering of nuclei, VL muscles increase nuclear DNA content; however in both systems, nuclei adjacent to the NMJ express specific genes required for NMJ function (Ganesan et al., 2011; Merlie and Sanes, 1985; Packard et al., 2015; Pavlath et al., 1989; B. Rosser and Bandman, 2003). Thus, it is likely that, as in mammals, NMJ and MTJs impose distinct functional requirements on adjacent VL nuclei. Further, it is possible that mechanical forces during muscle contraction have distinct affects along each cell. Experiments aimed at identifying the molecular mechanisms regulating the intracellular patterning and scaling relationships are underway and will provide valuable insights to the biology and physiology of muscle cells.

According to the myonuclear domain hypothesis, muscle fibers are composed of a mosaic of cytoplasmic domains, each regulated by a single nucleus (Hall and Ralston, 1989; Pavlath et al., 1989; Van der Meer et al., 2011). This concept of intracellular organization proposes that nuclei act mostly autonomously, with little exchange of gene products between neighboring nuclei. In contrast, the global nuclear scaling relationships uncovered in our study suggest that size regulation is highly coordinated among the nuclei contained within a VL muscle fiber. First, our data indicate that VL muscle nuclei are actively positioned via mechanical forces and based on cell geometries. Corresponding findings in mouse muscle fibers suggest that the mechanisms of nuclear positioning are conserved across species (Bruusgaard et al., 2003) and determine the relative spatial responsibility of individual nuclei. Further, our space-sensing model implicates the existence of a signaling molecule that diffuses across myonuclear domain boundaries to regulate individual nuclear sizes. In accordance with these simulations, increases and decreases in global DNA content affect absolute nuclear sizes, while nuclear positioning and the relative distribution of nuclear sizes within the cell is maintained. Together these data indicate that VL muscle fibers do establish distinct myonuclear domains; however, the mechanisms of intracellular size regulation determine the relative, rather than the absolute, contribution of individual nuclei

within a muscle syncytium.

Studies investigating the molecular mechanisms of intracellular size regulation in various mononucleated cell types have implicated the nucleolar protein Fibrillarin as a possible evolutionarily conserved molecular size sensor (Ma et al., 2016; Yi et al., 2015). As membrane-less organelles, nucleoli form via phase separation, and their size is determined by the concentration of nucleolar components inside the nucleus (Brangwynne, 2013). Strikingly, genetic manipulations of cell size at a fixed amount of nucleolar components in *C. elegans* embryos revealed inverse size scaling of nucleoli, so that nucleolar size was increased in smaller cells and decreased in larger cells (Weber and Brangwynne, 2015). Based on these and other findings it has been proposed that concentration-dependent inverse nucleolar scaling could serve as a link between cell size, nuclear size, and synthetic activity. If muscle nuclei contribute to a shared pool of nucleolar components, like Fibrillarin, which distribute throughout the cytoplasm, smaller nuclei containing less DNA would import a proportionally increased number of nucleolar components and form proportionally larger nucleoli. Indeed, our data show that small VL nuclei with low ploidy, contain proportionally bigger nucleoli that big nuclei within the same cell. We propose that, similar to mononucleated cells, nuclear and nucleolar sizes in VL muscles fibers are a linked via inverse scaling of the nucleolus. In a shared cytoplasmic space, this mechanism would allow for local differences in nuclear sizes and DNA content, while maintaining similar cytoplasmic domain sizes along each muscle fiber and stable global cell size regulation.

During muscle growth, increases in DNA content through endoreplication (*Drosophila*) or fusion (vertebrates), in transcriptional output, and in cytoplasmic domain sizes contribute to cellular hypertrophy (e.g. this work; (Kirby et al., 2016; Murach et al., 2018b; Qaisar and Larsson, 2014) . While domain sizes grow continuously, DNA content increases in steps, which requires, in theory, that nuclear activity is adjusted to compensate. Changes in cytoplasmic domain sizes have been observed in many growing vertebrate muscles (Murach et al., 2018a); however, how local nuclear synthetic activities correlated with these changes have not been analyzed in detail in whole muscle cells. Our genetic manipulations revealed which size parameters are linked and which are flexible and can compensate for changes in DNA content. Cdt1(Dup)KD nuclei increased nuclear areas despite reduced DNA content and smaller nucleoli; these data suggest changes in nuclear organization, such as chromatin organization, to overcome limitations to the synthetic machinery. MycOE muscle nuclei, in contrast, maintained the ratio of DNA per nuclear

area. However, these nuclei lost cumulative nuclear size scaling with cell size (that is, smaller muscle cells than would be predicted) as well as the local coordination of nuclear and nucleolar size scaling. Overall, our data also revealed a surprising dominance of systemic size regulators, such as growth factors (Demontis and Perrimon, 2009), to fulfill the requirements for a specific muscle size. As a consequence, different intracellular phenotypes (different local scaling along the fiber) developed. *Drosophila* larvae allow for easy, muscle-specific manipulations, and readouts of muscle function, which opens the door for future studies linking specific muscle phenotypes to pathways of intracellular size regulation and to functional consequences.

Using *Drosophila* larval VL muscles allowed us to perform a relatively straight-forward 2D quantification of muscle cell sizes and nuclear content. However, most vertebrate muscle fibers are cylindrical in shape with nuclei positioned along the entire fiber at the cell periphery. In addition, *Drosophila* larval muscle nuclei undergo endoreplication to increase DNA content during muscle growth, while in mice, increasing domain sizes during muscle growth (hypertrophy) can trigger increases in DNA content via cell fusion (Murach et al., 2018a; Qaisar and Larsson, 2014). Despite these differences, vertebrate and *Drosophila* muscles share many structural and functional similarities, which makes our study a suitable framework for understanding size control in different muscle systems. Further, the presence of increased nuclear DNA content has been shown in many differentiated cell types as common mechanisms to achieve large cell sizes (Orr-Weaver, 2015), making it worth testing whether vertebrate muscle nuclei actually maintain a diploid (2c) state. While the molecular mechanisms of intracellular size regulation in muscle fibers await further investigation, our study represents an important step toward optimizing the quantification of muscle cell size and understanding the complex mechanisms of size regulation in multinucleated cells. In this regard, our data should also inform size regulation in other multinucleated cell types such as trophoblasts and osteoclasts and affect our thinking on therapies aimed at affecting muscle growth, homeostasis, and regeneration. Ultimately, identifying the regulatory network that coordinates intracellular size regulation in multinucleated muscle fibers will reveal how disruption of sub-cellular organization results in muscle disease and reduced muscle function.

Acknowledgements

We would like to thank Terry Orr-Weaver, Norbert Perrimon, and the Bloomington Stock Center for flies. We acknowledge Raya Khanin in the MSKCC Bioinformatics core for the PCA analysis. We would also like to thank members of the Baylies Lab for helpful discussion, and particularly Mafalda Azevedo for critical reading of the manuscript. This work was supported by the NIH [GM121971, AR068128] to MKB and National Cancer Institute [P30 CA 008748] core grant to MSKCC. The funders had no role in the study design, data collection and analysis, decision to publish, or preparation of the manuscript.

Author contributions

S.W., M.B., A.M., and A.M. conceived the experiments; S.W. and A.M. carried them out; S.W. and A.M., with input from A.M. and M.B., designed and carried out the data analysis; A.B. and S.W. automated the larval data analysis; A.B. performed area/volume analysis. S.W., A.M., A.M., and M.B. prepared the manuscript.

Competing interests

We have no competing interests to declare.

References

Amodeo, A.A., Skotheim, J.M., 2016. Cell-Size Control. Cold Spring Harbor Perspectives in Biology 8, a019083. doi:10.1101/cshperspect.a019083

Boros, I.M., 2012. Histone modification in drosophila. Briefings in Functional Genomics 11, 319–331. doi:10.1093/bfgp/els029

Boulan, L., Milán, M., Léopold, P., 2015. The Systemic Control of Growth. Cold Spring Harbor Perspectives in Biology a019117–30. doi:10.1101/cshperspect.a019117

Brangwynne, C.P., 2013. Phase transitions and size scaling of membrane-less organelles. The Journal of cell biology 203, 875–881. doi:10.1083/jcb.201308087

Bruusgaard, J.C., Liestøl, K., Ekmark, M., Kollstad, K., Gundersen, K., 2003. Number and spatial distribution of nuclei in the muscle fibres of normal mice studied in vivo. The Journal of Physiology 551, 467–478. doi:10.1113/jphysiol.2003.045328

Chan, Y.-H.M., Marshall, W.F., 2012. How cells know the size of their organelles. Science (New York, N.Y.) 337, 1186–1189. doi:10.1126/science.1223539

Conklin, E.G., 1912. Cell size and nuclear size. Journal of Experimental Zoology 12, 1–98. doi:10.1002/jez.1400120102

Dej, K.J., Spradling, A.C., 1999. The endocycle controls nurse cell polytene chromosome structure during Drosophila oogenesis. Development 126, 293–303.

Demontis, F., Perrimon, N., 2009. Integration of Insulin receptor/Foxo signaling and dMyc activity during muscle growth regulates body size in Drosophila. Development (Cambridge, England) 136, 983–993. doi:10.1242/dev.027466

Demontis, F., Piccirillo, R., Goldberg, A.L., Perrimon, N., 2013. Mechanisms of skeletal muscle aging: insights from Drosophila and mammalian models. Dis Model Mech 6, 1339–1352. doi:10.1242/dmm.012559

Deng, S., Azevedo, M., Baylies, M., 2017. Acting on identity: Myoblast fusion and the formation of the syncytial muscle fiber. Seminars in Cell & Developmental Biology 72, 45–55. doi:10.1016/j.semcdb.2017.10.033

Dobi, K.C., Schulman, V.K., Baylies, M.K., 2015. Specification of the somatic musculature in Drosophila. Wiley interdisciplinary reviews. Developmental biology 4, 357–375. doi:10.1002/wdev.182

Du, Q., Gunzburger, M., Ju, L., 2010. Advances in studies and applications of Centroidal Voronoi tessellations. Numerical Mathematics 3, 119–142. doi:10.4208/nmtma.2010.32s.1

Eaton, M.L., Prinz, J.A., MacAlpine, H.K., Tretyakov, G., Kharchenko, P.V., MacAlpine, D.M., 2011. Chromatin signatures of the Drosophila replication program. Genome Research 21, 164–174. doi:10.1101/gr.116038.110

Figeac, N., Jagla, T., Aradhya, R., Da Ponte, J.P., Jagla, K., 2010. Drosophila adult muscle precursors form a network of interconnected cells and are specified by the rhomboid-triggered EGF pathway. Development (Cambridge, England) 137, 1965–1973. doi:10.1242/dev.049080

Folker, E.S., Baylies, M.K., 2013. Nuclear positioning in muscle development and disease. Front Physiol 4, 363. doi:10.3389/fphys.2013.00363

Frawley, L.E., Orr-Weaver, T.L., 2015. Polyploidy. Curr. Biol. 25, R353–8. doi:10.1016/j.cub.2015.03.037

Ganesan, S., Karr, J.E., Featherstone, D.E., 2011. Drosophila glutamate receptor mRNA expression and mRNP particles. RNA Biol 8, 771–781. doi:10.4161/rna.8.5.16014

Gillooly, J.F., Hein, A., Damiani, R., 2015. Nuclear DNA Content Varies with Cell Size across Human Cell Types. Cold Spring Harbor Perspectives in Biology 7, a019091–28. doi:10.1101/cshperspect.a019091

Ginzberg, M.B., Kafri, R., Kirschner, M., 2015. Cell biology. On being the right (cell) size. Science (New York, N.Y.) 348, 1245075–1245075. doi:10.1126/science.1245075

Grewal, S.S., Li, L., Orian, A., Eisenman, R.N., Edgar, B.A., 2005. Myc-dependent regulation of ribosomal RNA synthesis during Drosophila development. Nature cell biology 7, 295–302. doi:10.1038/ncb1223

Gundersen, G.G., Worman, H.J., 2013. Nuclear Positioning. Cell 152, 1376–1389. doi:10.1016/j.cell.2013.02.031

Gundersen, K., 2016. Muscle memory and a new cellular model for muscle atrophy and hypertrophy. J. Exp. Biol. 219, 235–242. doi:10.1242/jeb.124495

H Keshishian, K Broadie, A Chiba, A., Bate, M., 2003. The Drosophila Neuromuscular Junction: A Model System for Studying Synaptic Development and Function. http://dx.doi.org/10.1146/annurev.ne.19.030196.002553 19, 545–575. doi:10.1146/annurev.ne.19.030196.002553

Hall, Z.W., Ralston, E., 1989. Nuclear domains in muscle cells. Cell 59, 771–772. doi:10.1016/0092-8674(89)90597-7

Jevtić, P., Levy, D.L., 2014. Mechanisms of nuclear size regulation in model systems and cancer. Advances in experimental medicine and biology 773, 537–569. doi:10.1007/978-1-4899-8032-8_25

Kirby, T.J., Patel, R.M., McClintock, T.S., Dupont-Versteegden, E.E., Peterson, C.A., McCarthy, J.J., 2016. Myonuclear transcription is responsive to mechanical load and DNA content but uncoupled from cell size during hypertrophy. Molecular Biology of the Cell 27, 788–798. doi:10.1091/mbc.E15-08-0585

Levy, D.L., Heald, R., 2012. Mechanisms of intracellular scaling. Annual Review of Cell and Developmental Biology 28, 113–135. doi:10.1146/annurev-cellbio-092910-154158

Losick, V.P., Fox, D.T., Spradling, A.C., 2013. Polyploidization and cell fusion contribute to wound healing in the adult Drosophila epithelium. Curr. Biol. 23, 2224–2232. doi:10.1016/j.cub.2013.09.029

Losick, V.P., Jun, A.S., Spradling, A.C., 2016. Wound-Induced Polyploidization: Regulation by Hippo and JNK Signaling and Conservation in Mammals. PloS one 11, e0151251–20. doi:10.1371/journal.pone.0151251

Ma, T.-H., Lee, L.-W., Lee, C.-C., Yi, Y.-H., Chan, S.-P., Tan, B.C.-M., Lo, S.J., 2016. Genetic control of nucleolar size: An evolutionary perspective. Nucleus 7, 112–120. doi:10.1080/19491034.2016.1166322

Malfatti, E., Romero, N.B., 2017. Diseases of the skeletal muscle. Handb Clin Neurol 145, 429–451. doi:10.1016/B978-0-12-802395-2.00030-4

Manhart, A., Windner, S., Baylies, M., Mogilner, A., 2018. Mechanical positioning of multiple nuclei in muscle cells. PLoS Comput Biol 14, e1006208. doi:10.1371/journal.pcbi.1006208

Merlie, J.P., Sanes, J.R., 1985. Concentration of acetylcholine receptor mRNA in synaptic regions of adult muscle fibres. Nature 317, 66–68.

Metzger, T., Gache, V., Xu, M., Cadot, B., Folker, E.S., Richardson, B.E., Gomes, E.R., Baylies, M.K., 2012. MAP and kinesin-dependent nuclear positioning is required for skeletal muscle function. Nature 484, 120–124. doi:10.1038/nature10914

Miettinen, T.P., Pessa, H.K.J., Caldez, M.J., Fuhrer, T., Diril, M.K., Sauer, U., Kaldis, P., Björklund, M., 2014. Identification of Transcriptional and Metabolic Programs Related to Mammalian Cell Size. Current Biology 24, 598–608. doi:10.1016/j.cub.2014.01.071

Mukherjee, R.N., Chen, P., Levy, D.L., 2016. Recent advances in understanding nuclear size and shape. Nucleus 7, 167–186. doi:10.1080/19491034.2016.1162933

Murach, K.A., Englund, D.A., Dupont-Versteegden, E.E., McCarthy, J.J., Peterson, C.A., 2018a. Myonuclear Domain Flexibility Challenges Rigid Assumptions on Satellite Cell Contribution to Skeletal Muscle Fiber Hypertrophy. Front Physiol 9, 635. doi:10.3389/fphys.2018.00635

Murach, K.A., Fry, C.S., Kirby, T.J., Jackson, J.R., Lee, J.D., White, S.H., Dupont-Versteegden, E.E., McCarthy, J.J., Peterson, C.A., 2018b. Starring or Supporting Role? Satellite Cells and Skeletal Muscle Fiber Size Regulation. Physiology (Bethesda) 33, 26–38. doi:10.1152/physiol.00019.2017

Neumüller, R.A., Gross, T., Samsonova, A.A., Vinayagam, A., Buckner, M., Founk, K., Hu, Y., Sharifpoor, S., Rosebrock, A.P., Andrews, B., Winston, F., Perrimon, N., 2013. Conserved regulators of nucleolar size revealed by global phenotypic analyses. Science signaling 6, ra70–ra70. doi:10.1126/scisignal.2004145

Nordman, J., Li, S., Eng, T., Macalpine, D., Orr-Weaver, T.L., 2011. Developmental control of the DNA replication and transcription programs. Genome Research 21, 175–181. doi:10.1101/gr.114611.110

Packard, M., Jokhi, V., Ding, B., Ruiz-Cañada, C., Ashley, J., Budnik, V., 2015. Nucleus to Synapse Nesprin1 Railroad Tracks Direct Synapse Maturation through RNA Localization. Neuron 86, 1015–1028. doi:10.1016/j.neuron.2015.04.006

Pavlath, G.K., Rich, K., Webster, S.G., Blau, H.M., 1989. Localization of muscle gene products in nuclear domains. Nature 337, 570–573. doi:10.1038/337570a0

Peng, J.C., Karpen, G.H., 2007. H3K9 methylation and RNA interference regulate nucleolar organization and repeated DNA stability. Nature cell biology 9, 25–35. doi:10.1038/ncb1514

Penzo-Méndez, A.I., Stanger, B.Z., 2015. Organ-Size Regulation in Mammals. Cold Spring Harbor Perspectives in Biology 7, a019240–13. doi:10.1101/cshperspect.a019240

Piccirillo, R., Demontis, F., Perrimon, N., Goldberg, A.L., 2014. Mechanisms of muscle growth and atrophy in mammals and Drosophila. Dev. Dyn. 243, 201–215. doi:10.1002/dvdy.24036

Pierce, S.B., Yost, C., Britton, J.S., Loo, L.W.M., Flynn, E.M., Edgar, B.A., Eisenman, R.N., 2004. dMyc is required for larval growth and endoreplication in Drosophila. Development (Cambridge, England) 131, 2317–2327. doi:10.1242/dev.01108

Qaisar, R., Larsson, L., 2014. What determines myonuclear domain size? Indian J. Physiol. Pharmacol. 58, 1–12.

Ranganayakulu, G., Elliott, D.A., Harvey, R.P., Olson, E.N., 1998. Divergent roles for NK-2 class homeobox genes in cardiogenesis in flies and mice. Development 125, 3037–3048. doi:10.1101/gad.7.7b.1325

Roman, W., Gomes, E.R., 2017. Nuclear positioning in skeletal muscle. Seminars in Cell & Developmental Biology. doi:10.1016/j.semcdb.2017.11.005

Rosser, B., Bandman, E., 2003. Heterogeneity of protein expression within muscle fibers. American Society of Animal Science. doi:10.2527/2003.8114_suppl_2E94x

Rosser, B.W.C., Dean, M.S., Bandman, E., 2002. Myonuclear domain size varies along the lengths of maturing skeletal muscle fibers. Int. J. Dev. Biol. 46, 747–754.

Rudra, D., Warner, J.R., 2004. What better measure than ribosome synthesis? Genes & development 18, 2431–2436. doi:10.1101/gad.1256704
Schreiber, K.H., Kennedy, B.K., 2013. When lamins go bad: nuclear structure and disease. Cell 152, 1365–1375. doi:10.1016/j.cell.2013.02.015
Schulman, V.K., Dobi, K.C., Baylies, M.K., 2015. Morphogenesis of the somatic musculature in Drosophila melanogaster. Wiley interdisciplinary reviews. Developmental biology 4, 313–334. doi:10.1002/wdev.180
Sher, N., Stetina, Von, J.R., Bell, G.W., Matsuura, S., Ravid, K., Orr-Weaver, T.L., 2013. Fundamental differences in endoreplication in mammals and Drosophila revealed by analysis of endocycling and endomitotic cells. Proceedings of the National Academy of Sciences of the United States of America 110, 9368–9373. doi:10.1073/pnas.1304889110
Spradling, A., Orr-Weaver, T., 1987. Regulation of DNA replication during Drosophila development. Annu. Rev. Genet. 21, 373–403. doi:10.1146/annurev.ge.21.120187.002105
Team, R.C., 2013. R: A language and environment for statistical computing.
Unhavaithaya, Y., Orr-Weaver, T.L., 2012. Polyploidization of glia in neural development links tissue growth to blood-brain barrier integrity. Genes & development 26, 31–36. doi:10.1101/gad.177436.111
Uppaluri, S., Weber, S.C., Brangwynne, C.P., 2016. Hierarchical Size Scaling during Multicellular Growth and Development. CellReports 17, 345–352. doi:10.1016/j.celrep.2016.09.007
Van der Meer, S.F.T., Jaspers, R.T., Degens, H., 2011. Is the myonuclear domain size fixed? Journal of musculoskeletal & neuronal interactions 11, 286–297.
Weber, S.C., Brangwynne, C.P., 2015. Inverse size scaling of the nucleolus by a concentration-dependent phase transition. Curr. Biol. 25, 641–646. doi:10.1016/j.cub.2015.01.012
Whittaker, A.J., Royzman, I., Orr-Weaver, T.L., 2000. Drosophila double parked: a conserved, essential replication protein that colocalizes with the origin recognition complex and links DNA replication with mitosis and the down-regulation of S phase transcripts. Genes & development 14, 1765–1776.
Yi, Y.-H., Ma, T.-H., Lee, L.-W., Chiou, P.-T., Chen, P.-H., Lee, C.-M., Chu, Y.-D., Yu, H., Hsiung, K.-C., Tsai, Y.-T., Lee, C.-C., Chang, Y.-S., Chan, S.-P., Tan, B.C.-M., Lo, S.J., 2015. A Genetic Cascade of let-7-ncl-1-fib-1 Modulates Nucleolar Size and rRNA Pool in Caenorhabditis elegans. PLoS genetics 11, e1005580. doi:10.1371/journal.pgen.1005580

Figure Legends

Figure 1. Quantification of cell and nuclear sizes in *Drosophila* larval body wall muscles.
(A) Flat prep of third instar *Drosophila* larva showing skeletal muscles (red, phalloidin) and nuclei (cyan, α-Lamin) in bilateral abdominal hemisegments 2-6; anterior, left. Dashed line indicates one abdominal hemisegment; white box indicates Ventral Longitudinal (VL) muscles 3 and 4.
(B) 3D rendering (top), optical cross section (middle), and flattened confocal z-stack (bottom) of VL3 and VL4 muscles.
(C) Schematics of the geometric shapes of VL muscle cells (top), and nuclei (middle). Green areas are quantified after z-projection of confocal stacks. Bottom, binary image of VL muscles and nuclei shown in Figure 1B.
(D,E) Scatter plots comparing volume and thickness (orange) measurements with the area (green) of individual VL muscle cells (D) and nuclei (E). Linear regression curves and correlations coefficients (R) are indicated. n (cells) = 42, n (nuclei) = 572.
(F,G) Median VL3 and VL4 cell areas (F) and nuclear numbers (G). Boxes, 25/75 percentiles; whiskers, min/max values. n_{VL3} = 102, n_{VL4}= 97. $p<0.0001$ (Student's t test).
(H) VL3 (black) and VL4 (gray) muscle areas plotted against the corresponding abdominal hemisegment of the larvae. Lines represent mean values. n_{VL3} = 102, n_{VL4} = 97.
(I) VL3 and VL4 muscles from different hemisegments within the same larva.
(J) Unsupervised multidimensional cluster analysis of VL muscles from 3 different genetic control backgrounds
(w^{1118}, *Dmef2-GAL4;UAS-2xEGFP*, *Dmef2-GAL4;UAS-GFP RNAi*, two experimental replicates each) using the following parameters: cell size, cell shape (aspect ratio), nuclear number, total nuclear area, axis level (abdominal hemisegment number). VL3 (black) and VL4 (gray) muscles form separate clusters with little overlap. See also Figure S1A. n_{VL3} = 102, n_{VL4} = 97.
Scale bars, 500 μm (A), 100μm (B), 50μm (I).

Figure 2. Muscle nuclei establish precise global scaling with cell size.
(A) VL3 muscles with similar areas but differences in nuclear number. Cells (phalloidin, red) and nuclei (Hoechst, gray) are outlined in cyan and yellow, respectively. Dashed lines highlight one nucleus each cell (right); nuclear size, DNA content and nucleolar size (Fibrillarin-1, cyan) are increased in the cell containing fewer nuclei (bottom).
(B) Staining of DNA (Hoechst, gray) in diploid (2c) adult muscle progenitors (AMPs, dashed oval) and polyploid VL muscle nuclei. Red, phalloidin; Yellow, Nucleus, α-Lamin.
(C) Left: labeling of nucleoli (α-Fibrillarin, cyan) and DNA (Hoechst, gray) in VL muscle nuclei. Right: binary image for quantification of areas.
(D-G) Nuclear number (D; n_{VL3}=102, n_{VL4}=97), cumulative DNA copy number (c)(E; n_{VL3}=67, n_{VL4}=75), cumulative nucleolar area (F; n_{VL3}=54, n_{VL4}=54), and cumulative nuclear area (G; n_{VL3}=102, n_{VL4}=97) plotted against muscle cell area. Bold lines and correlations coefficients (R) indicate linear scaling across VL3 (black) and VL4 (gray) muscles. Dashed lines indicate individual linear regressions for VL3 (blue) and VL4 (red) muscles. Cells with the same number of nuclei, e.g. 9 (red) and 15 (blue), achieve different cell sizes, and vary in their cumulative amount of nuclear DNA, nucleolar sizes and nuclear sizes.
(H,I) Global size parameters as in (D-G) normalized by the number of nuclei per cell
(H) Histogram of mean cytoplasmic domain sizes (cell area/nuclear number) in VL3 and VL4 muscles, showing similar "optimal" cytoplasmic domain size in both VL muscles (green area).

(I) Mean ploidy (cumulative DNA content/nuclear number), mean nuclear area (cumulative nuclear area/nuclear number), and mean nucleolar area (cumulative nucleolar area/nuclear number) plotted against the mean cytoplasmic domain size. Green area corresponds to optimal cytoplasmic domain size as in (H). Error bars, SD.
(J) Schematic representation of nuclear size scaling and nucleolar size scaling.
(K) Nuclear size scaling and nucleolar size scaling plotted against the average size of the cytoplasmic domains within VL3 cells (for VL4, see Figure S2I). Note: highest nuclear scaling values are associated with optimal cytoplasmic domain sizes (green area), while smaller or larger domain sizes correlate with increased nucleolar scaling and proportionally smaller nuclei.
Scale bars, 50µm (A), 25µm (B,C).

Figure 3. Nuclei are positioned via a force balance and individually adjust their sizes based on spatial cues
(A) Schematic representation of VL3 and VL4 muscles and nuclei, nuclear centroids, nearest neighbor distances (blue arrows) and cytoplasmic domain sizes (Voronoi tessellation, dashed lines).
(B) Histograms of relative nuclear positions along the short cell axis (A, bottom right). Real data (green lines) and simulated nuclear positions (dashed lines) show organization in one or two rows for each muscle type. For simulation details see methods.
(C) Nuclear positioning as a function of nuclear number (left) and cell width (right). For each cell the average position of all nuclei to either side of the cell midline was plotted (experimental data in green, simulated data in black). Thick lines and shaded regions show means, SD; each dot represents one cell (VL3 blue, VL4, red).
(D) Simulation of nuclear positioning. Top: Schematic representation of the potential mechanical pushing forces between nuclei and cell edges (left) and between neighboring nuclei (right). Lines represent microtubules, green circles nuclei, arrows indicate the resulting forces. Middle: Cell outline (black) and nuclear positions (green circles) of one example VL3 cell. Arrows represent forces felt by the nucleus marked with a black outline from neighboring nuclei (dark gray arrows) and cell edges (light gray arrows). Arrow widths represents force strength. Bottom: For the example cell above, initial nuclear positions (measured, green circles) and final force-balanced positions (simulated, black circles) are shown. For simulation details see Suppl. Methods.
(E) Simulation of nuclear space-sensing. Top: Nuclear positions, sizes, and shapes (green discs, using fitted ellipses) of one example VL3 cell. The orange particle represents one modeled space-sensing molecule. Middle: Final distribution of the space-sensing molecule as simulated for the example cell above (blue=zero concentration, red=maximal concentration). Bottom: Measured and simulated nuclear areas for the example cell above. Nuclei are indexed from left to right as indicated at the top. For simulation details see Suppl. Methods.
(F) Scatter plot showing correlation of real nuclear areas with nuclear areas predicted by simulation of local size sensing. Inset (top) shows representative simulation result; colors indicate concentration of a hypothetical cytoplasmic molecule which is absorbed by each nucleus (white circles).
(G-J) Thick lines and shaded regions show means, SD; each dot represents one cell (VL3 blue, VL4, red).
(G) Linear correlation of nuclear areas with Voronoi domain areas ($R=0.55$, $p<0.0001$).
(H) Distribution of normalized Voronoi domain size (Voronoi Area*No. of Nuclei/Cell Area) along the cell length. Thick lines show averages, shaded regions correspond to standard deviation.

(I) Distribution of normalized nuclear areas (Nuclear Area*No. of Nuclei/Total Nuclear Area) along the cells showing largest nuclei in the cell middle. VL3 nuclei (mean+/-SD = 202+/-55um) are larger than in VL4 nuclei (192+/-44um).
(J) Multiple Linear Regression showing that Voronoi area (nVD=normalized Voronoi Area) and nuclear position along the long cell axis (RY=absolute relative y-position, with 0=middle and 1=poles) give a good prediction of nuclear size ($R=0.66$, $p<0.0001$). Each dot represents one cell (VL3 blue, VL4, red).
Sample numbers: n (cells) = 200 (103 VL3, 97 VL4), n (nuclei) = 2477 (1579 VL3, 898 VL4).

Figure 4. Local nuclear size scaling and synthetic activity are inversely correlated.
(A) Positions of NMJ (α-Discs large, yellow) and MTJs (yellow arrowheads) in VL3 and VL4 muscles. Muscle, Red, phalloidin; nuclei, white, Hoechst; nucleolus, cyan, α-Fibrillarin.
(B) Scatter plot showing distribution of normalized local nuclear size scaling (ratio of nuclear area to Voronoi domain) along the length of VL muscle fibers ($n_{VL3}=57$, $n_{VL4}=61$ muscles). Highest values correlate with mean position of the NMJ (yellow; start: 29.03+/-4.48%, end: 53.74+/-7.88% of cell length; $n_{VL3}=24$, $n_{VL4}=24$). Error bars, SD.
(C) VL muscles nuclei containing 16, 32 or 64 copies (c) of DNA. See also Figures S2A-D.
(D) Frequency of 16c, 32c and 64c nuclei as a function of mean Voronoi domain size. The ratio of nuclear ploidy numbers in individual cells depends on nuclear number and cell size.
(E) Pie charts showing similar ratio of nuclear ploidies in VL3 and VL4 muscles.
(F) Histogram of nuclear ploidy numbers along the long cell axis (anterior left, posterior right). NMJ region noted by yellow box as in (B).
(G) Bar graph (mean +/- SD) comparing absolute size of Voronoi domain ($p<0.0001$), nuclear area ($p<0.0001$) and nucleolar area ($p<0.0001$), and size scaling of nuclei ($p=0.0009$) and nucleoli ($p<0.0001$) in nuclei with 32 and 64 copies of nuclear DNA. Means for 32c nuclei were set to 100%.
(H) Nuclear size scaling (nuclear per Voronoi area) along the length of VL muscle fibers. DNA copy number for each nucleus plotted. NMJ position is indicated in yellow error bars as in (B).
(I) Representative images showing nucleoli (Fibrillarin-1, green), H3K9ac (magenta) and DNA (Hoechst, gray) in polyploid VL nuclei.
(J) Normalized nucleolar areas plotted against cell length. Mean values for nuclei with 32c and 64c, and VL3 and VL4 muscles are indicated. Black line shows normalized DNA content for reference. NMJ region (yellow box) as in (B).
(K) Box plots (median, 25/75 percentile, min/max values) showing proportional increase of H3K9ac with DNA content thus similar relative values per nucleus, independent of absolute DNA content.
(L) Normalized H3K9ac intensity measurements plotted against cell length. Mean values for VL3 and VL4 muscles are indicated. Dark green line shows normalized DNA content for reference. NMJ region (yellow box) as in (B).
(M) Normalized nucleolar size scaling plotted against cell length. Mean values for nuclei with 32c and 64c, and VL3 and VL4 muscles are indicated. NMJ region (yellow box) and normalized nuclear size scaling (black line) as in (B).
(N) Schematic highlighting the inverse relationship of nuclear and nucleolar size scaling (as in (M)) at constant DNA content (see (L)) at the NMJ. Lower case letters (a, b, c; graph, left) reflect areas from which representative nuclei and nucleolar scaling relationships are depicted in drawing (a, b, c; right).

Scale bars: 50 μm (A), 25 μm (C,I).
Sample numbers: n=1286 nuclei (B,H,J,M,N), n=950 nuclei (D-G,K,L)

Figure 5. Muscle specific manipulations of nuclear DNA content.
(A) VL3 and VL4 with muscle-specific knockdown of Cdt1(Dup) (top) and overexpression of Myc (bottom). For representative control image see Figure 1B. Changes in nuclear DNA content (Hoechst, gray) and nucleolar sizes (α--Fibrillarin, cyan) are shown in panels in the middle and on the right, respectively. Muscle, phalloidin, red; nuclei, α-Lamin, cyan (left panel).
(B) Boxplot showing median VL3 cell areas and larval crawling velocities in Cdt1(Dup)KD, MycOE, and control larvae (boxes, 25/75 percentiles; whiskers, min/max values). Cell areas are only slightly reduced in Cdt1(Dup)KD (n=39 cells, p=0.1714) and unchanged in MycOE (n=18 cells, p=0.5760) when compared to control (n=28 cells). Larval crawling velocity in significantly reduced in Cdt1(Dup)KD (n=24 larvae, p=0.0044) as well as in MycOE (n=27 larvae, p=0.0017) compared to control (n=27 larvae). p values and asterisks indicate Student's t test results.
(C-F) Scatter plots showing scaling of nuclear number(C), cumulative DNA content(D), cumulative nucleolar area(E) and cumulative nuclear area (F) across VL 3 (filled symbols) and VL4 muscle types (outlined symbols) in Cdt1(Dup)KD (orange), MycOE (purple) and control muscles (black).
(G) Distribution of normalized nuclear areas along the length of each muscle fibers. Values are expressed as % deviation from average per genotype. Solid lines indicate mean. The distribution of nuclear areas in the Cdt1(Dup)KD and in MycOE is similar to control.
(H) Linear isometric scaling of cumulative nucleolar area with DNA content in Cdt1(Dup)KD muscles.
(I) Boxplot showing median nuclear and nucleolar scaling in Cdt1(Dup)KD, MycOE, and control larvae (boxes, 25/75 percentiles; whiskers, min/max values). *** indicates p values <0.0001 for all genotypes (Student's t test).
(J) Linear isometric scaling of cumulative nuclear area with DNA content in MycOE muscles.
(K,L) Normalized nuclear and nucleolar size scaling, and H3K9ac per Hoechst fluorescence intensity plotted along the length of Cdt1(Dup)KD and MycOE muscles. For wild-type patterns see Figure 4).
Sample numbers: Control, n_{VL3}=28, n_{VL4}=35 cells; Cdt1(Dup)KD, n_{VL3}=39, n_{VL4}=35 cells; MycOE, n_{VL3}=18, n_{VL4}=19 cells (C-J).

Figure 6. Levels of intracellular size regulation in multinucleated muscle fibers.

STAR Methods

CONTACT FOR REAGENT AND RESOURCE SHARING

Further information and request for resources and reagents should be directed to and will be fulfilled by the Lead Contact Mary K. Baylies (m-baylies@ski.mskcc.org).

EXPERIMENTAL MODEL AND SUBJECT DETAILS

Fly stocks and staging

The following *Drosophila* stocks were maintained under standard conditions on cornmeal medium: w^{1118} (Bloomington 3605), *Dmef2-GAL4* (Ranganayakulu et al., 1998), *UAS-2xEGFP* (Bloomington 6874), *UAS-GFP RNAi* (from J. Zallen, SKI), *UAS-dmyc* (from N. Perrimon), *UAS-dup (double parked/Ctd1) RNAi* (from T. Orr-Weaver). Crosses (GAL4 X UAS) were performed at 25 °C on apple juice plates under 12:12 Light:Dark conditions and constant humidity. For all experiments, embryos hatched within a 2h period were selected and raised to third instar larval stage on cornmeal medium at 25 °C. Staging of 3rd instar larvae was confirmed using developmental landmarks, including mouth hook and spiracle morphologies.

METHOD DETAILS

Dissections, labeling and confocal imaging

Wandering third instar larvae were dissected, fixed in 10% formalin and labeled as previously described (Metzger et al., 2012). Muscle cells were labeled using Alexa Fluor-conjugated phalloidin (Life Technologies). Anti-Lamin (ADL67.10, DSHB; 1:100), anti-Fibrillarin (MCA-38F3, EnCor; 1:100), anti-H3K9ac (Active Motif; 1:200), anti-discs large (4F3, DSHB; 1:200), anti-alpha tubulin (Sigma, 1:500) primary antibodies and Alexa Flour-conjugated secondary antibodies (Life Technologies; 1:200) were used to label cellular and nuclear structures. Hoechst 33342 (Invitrogen; 1 μg/ml) was used to label nuclear DNA. Whole larvae were mounted in ProlongGold (Invitrogen). VL3 and VL4 muscles in abdominal hemisegments 2-6 were imaged on a LSM 700 confocal microscope (Zeiss). All samples intended for direct comparison were imaged using the same confocal settings.

Image processing and measurements

All images were processed and analyzed using standard ImageJ (FIJI) measurement tools. For 2D quantification of VL3 and VL4 muscles, z-projections of confocal images were used. VL3 and VL4 cell areas were traced by hand, based on phalloidin labeling. Outlines were used to record shapes (aspect ratio; cell width/cell length), sizes (areas) and positions (coordinates) of individual cells. To determine NMJ length, we generated binary imaged of anti-discs large labeling and recorded area and position of the NMJ in relation to VL3 and VL4 cells. Automated thresholding of fluorescence intensities of anti-Lamin and/or Hoechst labeling was used to generate binary images of VL nuclei. We recorded the number, size (areas) and position (centroids) of all nuclei within each cell, and we used the binary images as masks to measure Hoechst and H3K9ac fluorescence intensities (sum intensity of pixel density) within those nuclei. Further, nuclear centroids were used to calculate nearest neighbor distances and perform Voronoi tessellation (Du et al., 2010). Automated thresholding of anti-Fibrillarin labeling was used to generate binary images of nucleoli and measure nucleolar sizes (areas). For calculation of DNA content, we normalized Hoechst fluorescence intensities of each muscle nucleus to diploid Adult Muscle Progenitors (AMPs) (Figeac et al., 2010) from the same larva. Work from the Orr-Weaver, Spradling, and others labs routinely use DNA stains to estimate DNA content and ploidy (e.g. (Dej and Spradling, 1999; Losick et al., 2013; 2016; Sher et al., 2013; Unhavaithaya and Orr-Weaver, 2012)). Note that the extent of genome replication in polyploid cells has been published for several *Drosophila* tissues; it is known that not all genomic sequences are equally replicated, as an example, the heterochromatin (20-30% of the genome) is not replicated in tissues like the larval salivary gland and midgut (Nordman et al., 2011). Likewise, it has been determined that in larval salivary gland cells, ovarian follicle cells, and pupal trichogen cells, but not nurse cells, that rRNA genes are not fully replicated. As an example, salivary gland cells contain only one-fourth to one-eighth the expected number of rRNA genes (reviewed in: (Spradling and Orr-Weaver, 1987)).

For 3D measurements of VL cell and nuclei, we determined the average depth/thickness of each cell and of all nuclei from one representative experiment. Volumes were calculated by multiplying thickness values with area measurements.

Simulation of random nuclear positioning

To simulate random positioning of nuclei within VL muscle fibers, we used actual cell parameters of 200 wild-type cells (width, height, number of nuclei) and positioned nuclei randomly following

uniform distributions. To assess the influence of stochasticity on our results, we repeated this procedure 1000 times. We calculated mean nearest neighbor distances and standard deviations for VL3 and VL4 nuclei +/- std. The fits of Gaussians to the data (thick lines) were computed using the measured mean and std of the data.

Simulation of nuclear positioning

We simulated the positioning of N equally sized nuclei in a rectangular domain that interact with each other and with the cell sides via an isotropic pushing force, decreasing with distance. To underscore the differences between VL3 and VL4 cells, only cells from hemisegments 1-4 were used. Since we are working in a low Reynolds number regime, we can assume a friction-dominated environment, i.e. the velocities of the nuclei are proportional to the forces acting on them. Since we are only interested in equilibrium positions, we can rescale in order to normalize the coefficient of the internuclear interactions to 1. We assume the position of the centroid of the i-th nucleus follows

$$\frac{d}{dt}X_i(t) = \sum_{j=1, j\neq i}^{N} f\left(d_{ij}\right)N_{ij} + \sum_{k=L,R,U,D}^{N} q\, f(d_{ik})N_{ik}$$

where d_{ij} is the distance between centroids i and j, N_{ij} is the vector of length 1 pointing from nucleus j to nucleus i. For the interactions with the sides, we define d_{ik} as the shortest distance between the i-th nucleus and the side with index k (L=left, R=right, U=upper, D=down) and N_{ik} is the unit vector normal to that side pointing towards the i-th nucleus. The scalar function f(d)>0 is a distance dependent pushing force and q is a free parameter describing the ratio between internuclear and nucleus-side forces. We used $f(d)=1/d$ and $f(d)=1/d^2$. To directly compare with the data, we used the same cell widths, heights and number of nuclei as measured for the experimental data. As initial conditions the real positions were used, since this allows the use of the mean distance between the real and final (equilibrium) positions of the nuclei as an error functional in the simulation. This error was minimized with respect to q. Here only the results using $f(d)=1/d^2$ are shown, which gave a better fit with the data. The error functional was minimal for q=0.7. To simulate, we used Matlab's ode solver *ode15*, a variable-step, variable-order solver.

Simulation of space-sensing

We simulated the distribution of a signaling molecule, that is produced at a constant rate everywhere in the cell and diffuses until it is absorbed by a nucleus. For each cell, the real geometry and nuclear positions were used with nuclear radii of 3.8µm. Mathematically, we solve the Poisson equation in 2D within each cell using Neumann boundary conditions at the cell membrane and Dirichlet boundary conditions at the nuclear envelope, i.e. if s(x) is the concentration of the signal at position x, we solve

$$\Delta s = -1, x \in C$$
$$s = 0, x \in \partial N$$
$$\nabla s.n = 0, x \in \partial C$$

where ∂Ndenotes the union of all the boundaries of all nuclei and $\partial C$is the cell boundary. We solve using a Finite Element Method with an adaptive mesh utilizing Matlab's PDE toolbox. The amount of signal each nucleus receives, S, was calculated as the integral of the fluxes at its boundary. We assumed a linear relationship between the amount of signal received and the area of the nucleus A:

$$A = A_{min} + \alpha S$$

We fitted the parameters A_{min} (the minimal nuclear area) and α (the sensitivity) to maximize the correlation between simulated and measured nuclear sizes, yielding A_{min}=83 µm^2 and α=0.044 µm^2 per unit signal.

Larval locomotion assay

Third instar larvae were placed in the center of a 10 cm apple juice plate (stained with green food color for better contrast) and recorded for 1 minute using an iPhone SE (Apple) on a custom mount. Each genotype was analyzed in 2 independent experiments; per individual experiment, a minimum of 10 larvae was analyzed. Movies of larval locomotion were processed and quantified in ImageJ using the trackmate plugin. Average velocities (+/- standard deviation) per genotype.

QUANTIFICATION AND STATISTICAL ANALYSIS

Sample sizes were chosen based on previous experience in the laboratory. Each experiment was performed in 2 technical replicas; per individual experiment a minimum of 4 larvae (biological replicates) and at least 8 VL muscles per larva were analyzed. For wild-type analyses, we quantified a total of 102 VL3 and 97 VL4 muscles from three control genotypes

(*w*^{1118}, *Dmef2-GAL4;UAS-2xEGFP*, *Dmef2-GAL4;UAS-GFP RNAi*). Two-tailed Student's *t*-test and correlation coefficients (R) were computed using GraphPad Prism version 7.0a for Mac (GraphPad Software).

Unsupervised multidimensional cluster analysis

Analysis was performed in R statistical language (Team, 2013). Data was clustered using classical multidimensional scaling (MDS) using cmdscale() function with Euclidean distances and default parameters.

Multiple linear regression analysis

To allow for direct comparison of the data and assess which parameters best predict nuclear sizes, we normalized all parameters (see below). The best prediction gave the following linear regression model: normalized (norm.) nuclear area = a + b (norm. Voronoi area) + c (norm. distance to center). Where norm. nuclear area = nuclear area divided by the mean nuclear area in each cell; norm. Voronoi area = Voronoi area divided by the mean Voronoi area in each cell; norm. distance to center is defined between 0 (center) and 1 (poles). We fitted coefficients a,b,c of the linear regression model, yielding a=0.87, b=0.31, c=-0.33. p-values are well below 1% for both variables. R^2=0.477. Note that norm. Voronoi area and norm. distance to center are not correlated with each other (R=-0.082).

KEY RESOURCES TABLE

REAGENT or RESOURCE	SOURCE	IDENTIFIER
Antibodies		
Mouse anti-Lamin	DHSB	ADL67.10
Mouse anti-Fibrillarin1	EnCore	MCA-38F3
Rabbit anti-H3K9ac	Active Motif	**Catalog No: 39138**
Mouse anti-Discs Large	DHSB	4F3
Mouse anti-alpha tubulin	Sigma	DM1A
Goat anti-mouse Alexa conjugated secondaries	Life Technologies	
Experimental Models: Organisms/Strains		
D. melanogaster: w1118	Bloomington Drosophila Stock Center	BDSC:3605
D. melanogaster: Dmef2-Gal4	(Ranganayakulu et al., 1998)	
D. melanogaster: UAS-2xEGFP	Bloomington Drosophila Stock Center	BDSC:6874
D. melanogaster: UAS-GFP RNAi	from J. Zallen (SKI)	
D. melanogaster: UAS-dmyc	from N. Perrimon	
D. melanogaster: UAS-dup (double parked/Cdt1) RNAi	from T. Orr-Weaver	
Software and Algorithms		
ImageJ/Fiji	Fiji	https://fiji.sc/
GraphPad Prism	GraphPad	https://www.graphpad.com/
Excel	Microsoft	https://products.office.com/en-us/excel
Matlab	Mathworks	https://www.mathworks.com/products/matlab.html
Imaris	Bitplane	http://www.bitplane.com/imaris/imaris
R	R Foundation for Statistical Computing	https://www.r-project.org/
Cytosim	Nédélec Laboratory	http://github.com/nedelec/cytosim
Illustrator	Adobe	www.adobe.com

Figure 1.

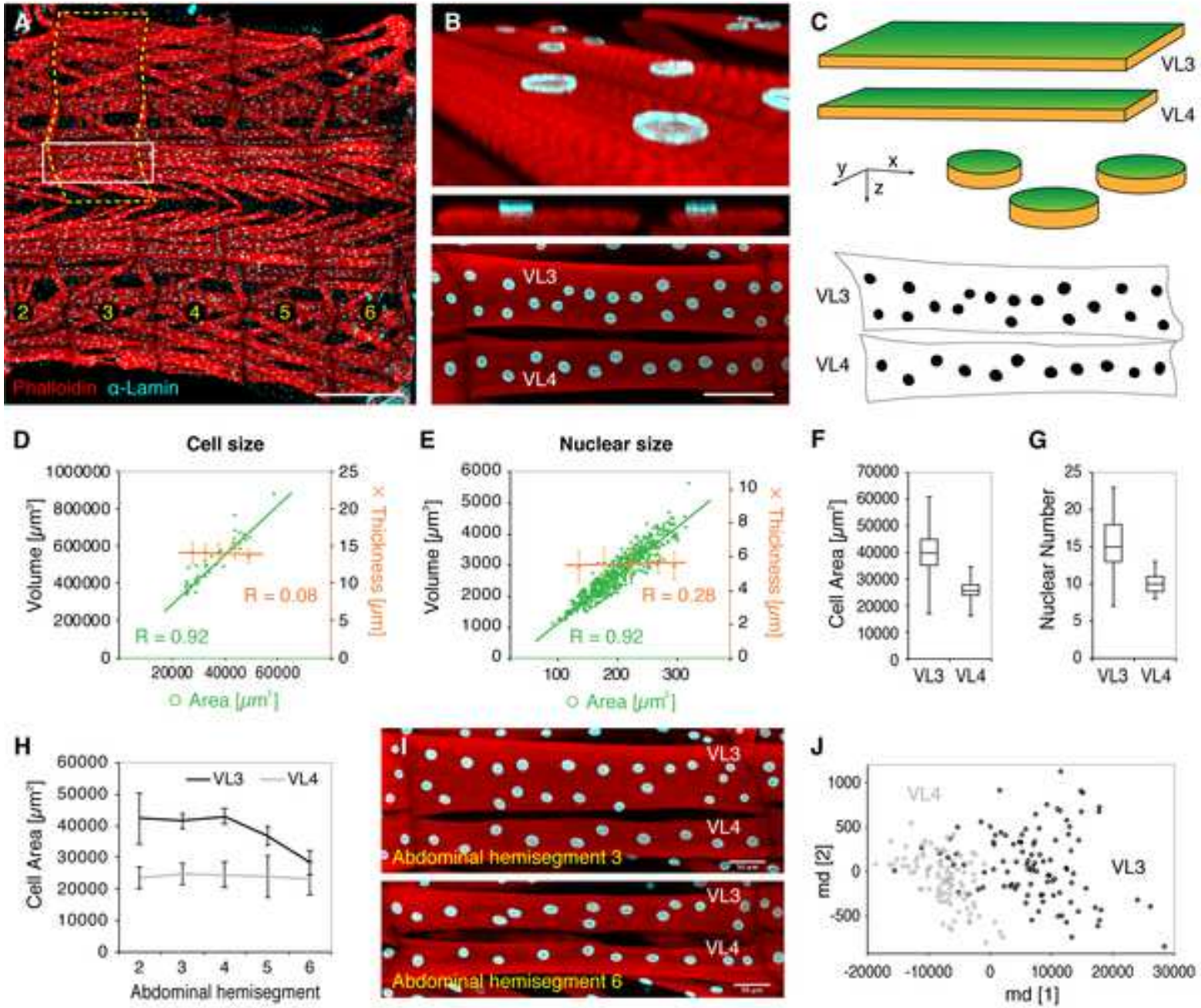

Figure 2.

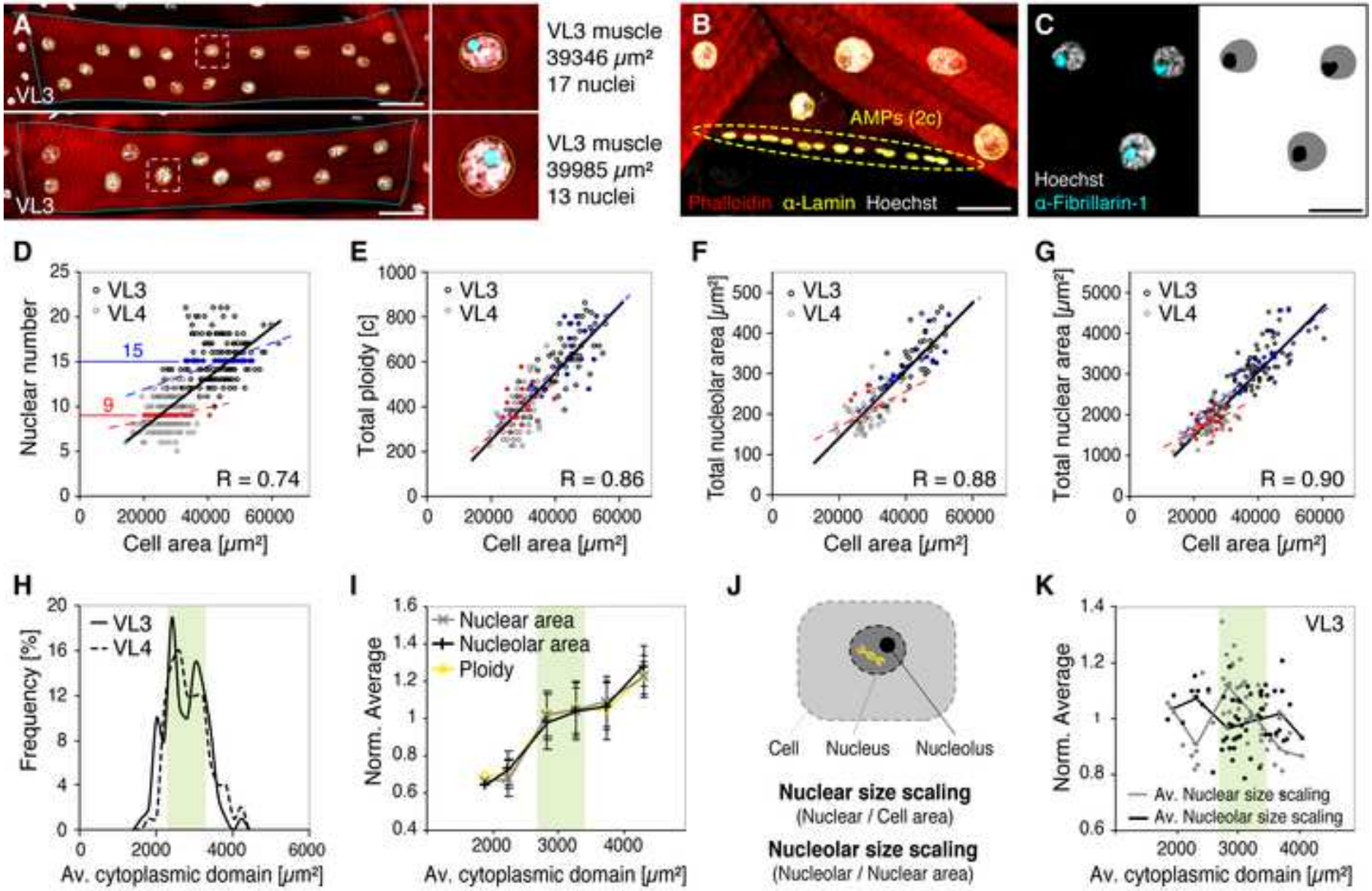

Figure 3.

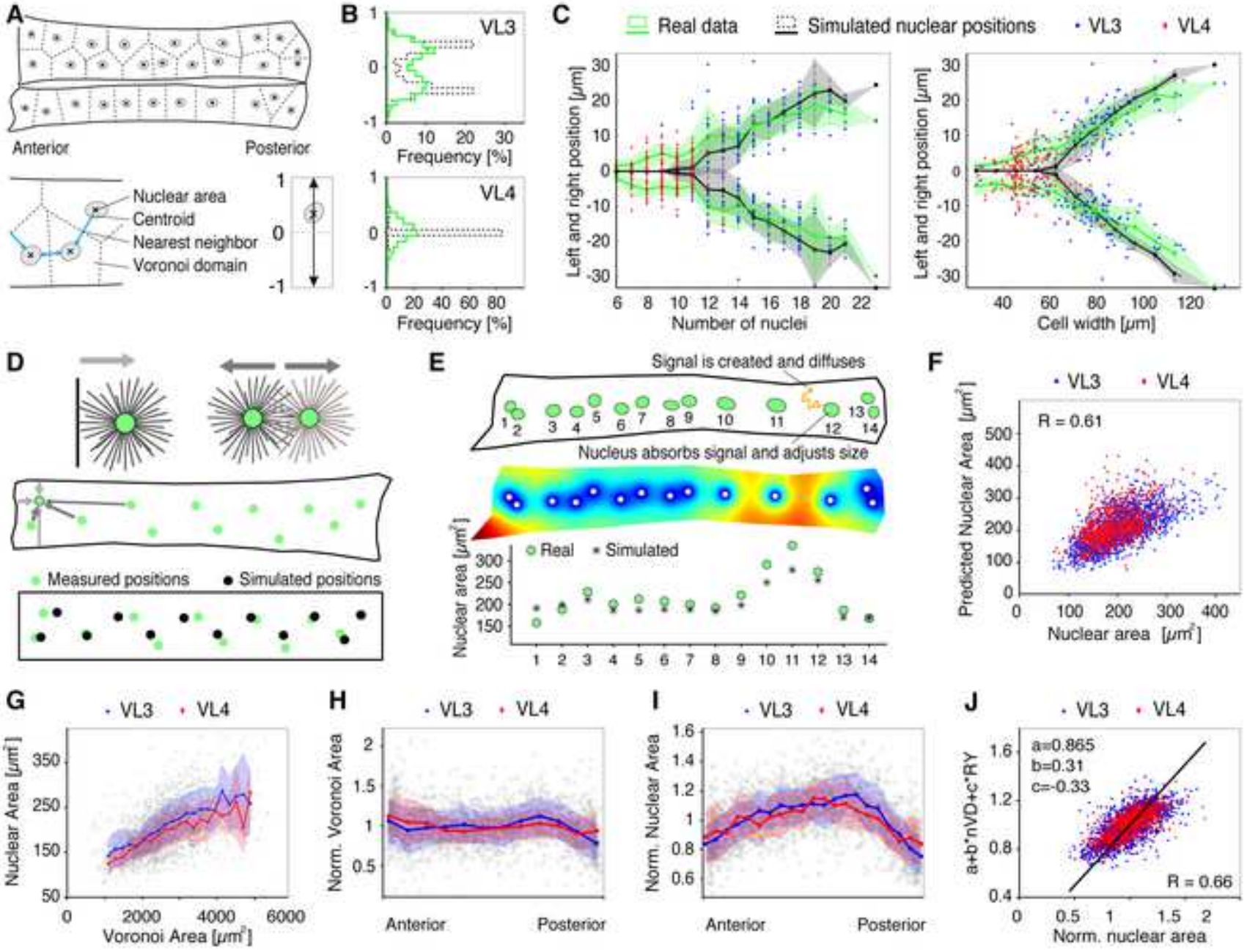

Figure 4.

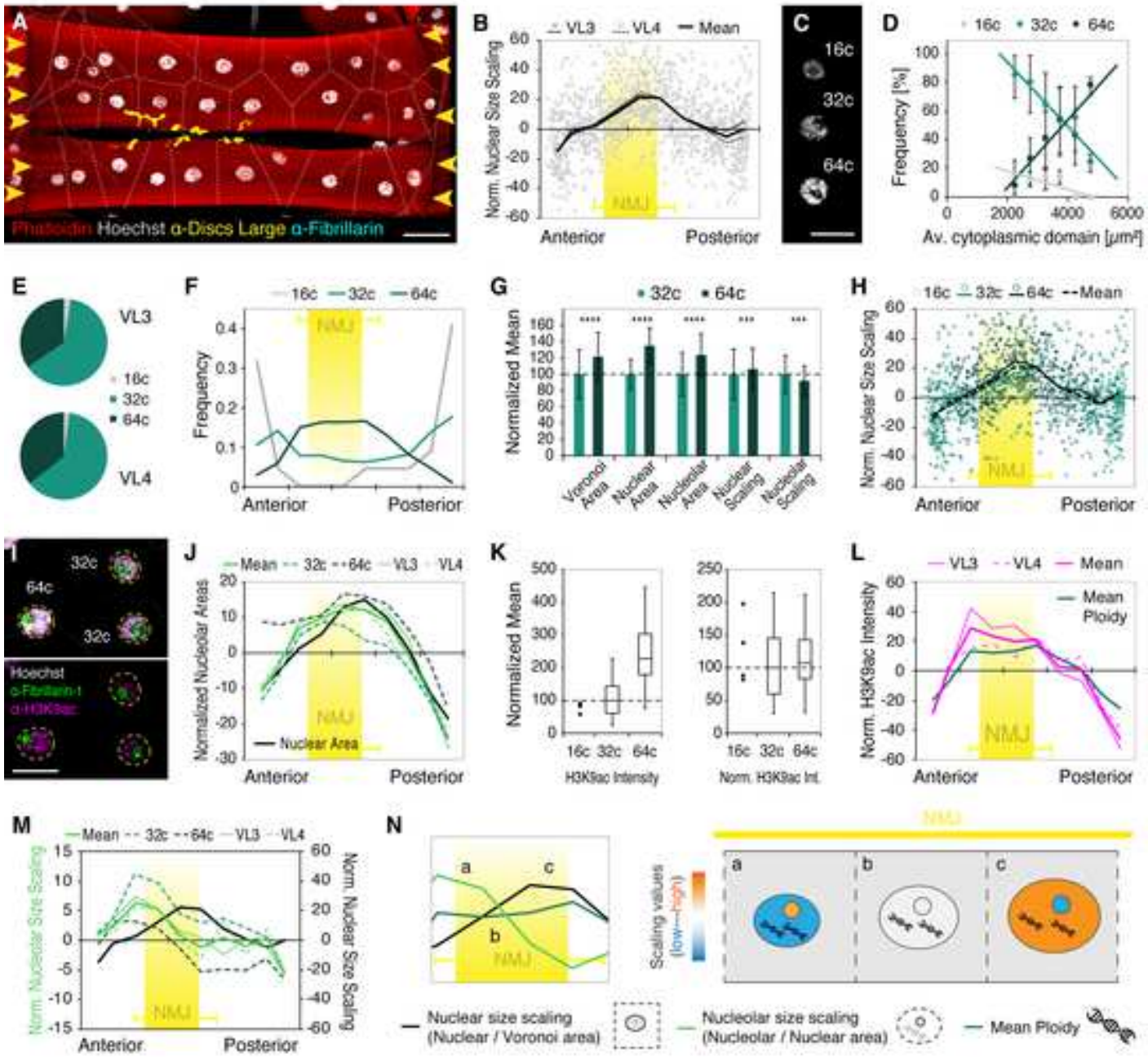

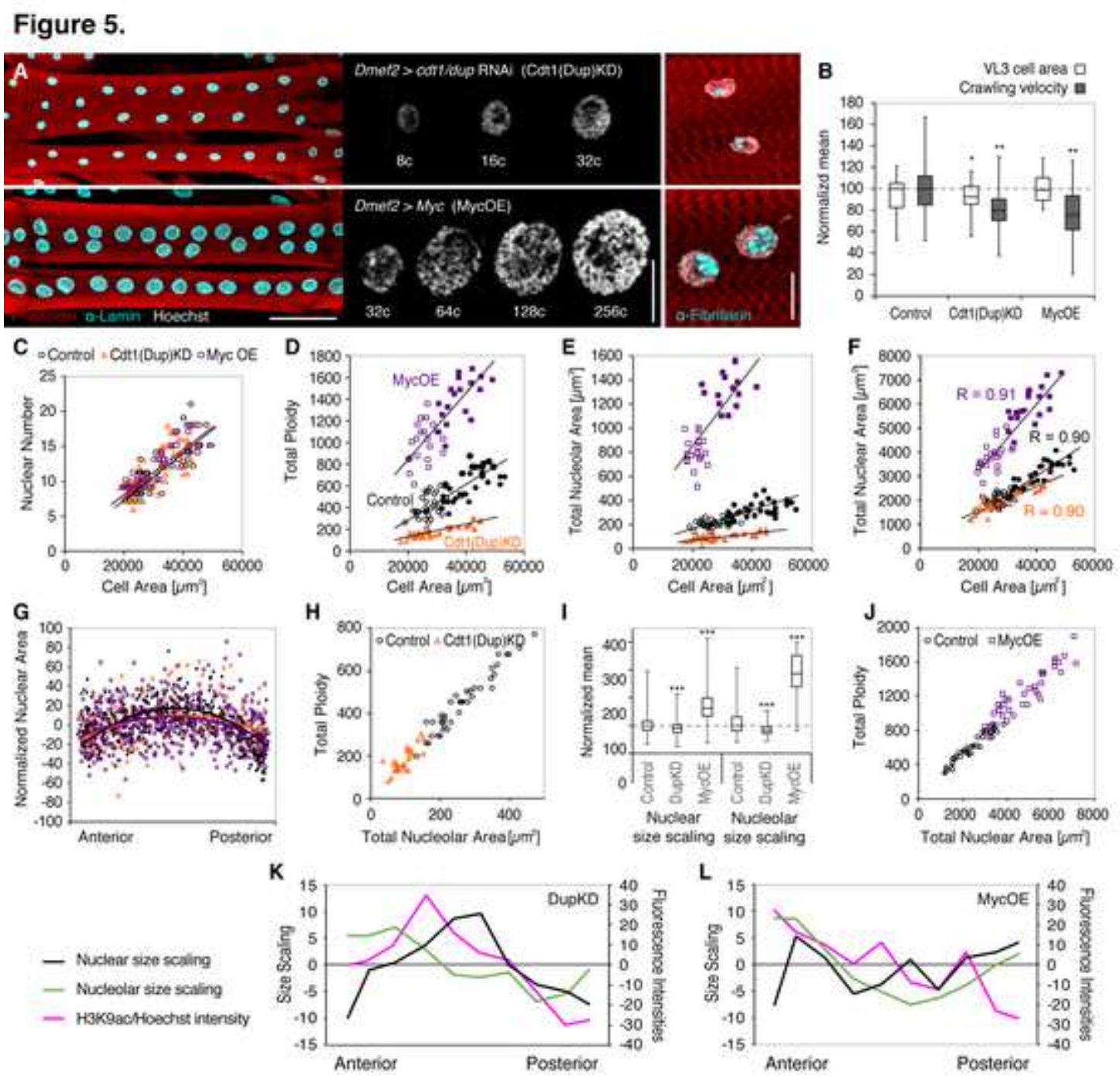

Figure 6

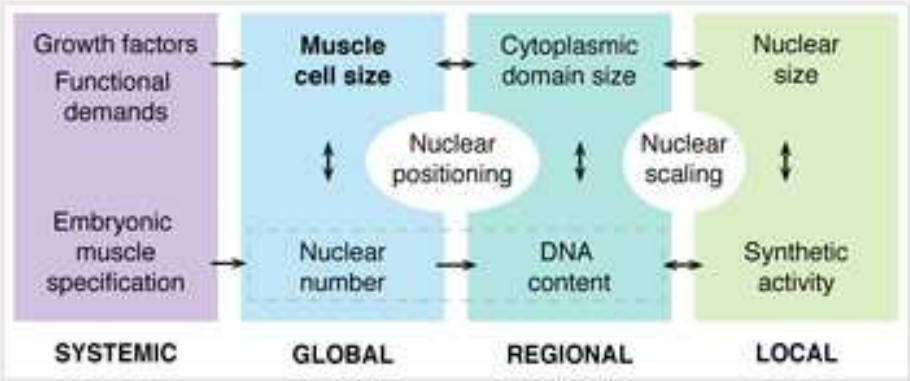

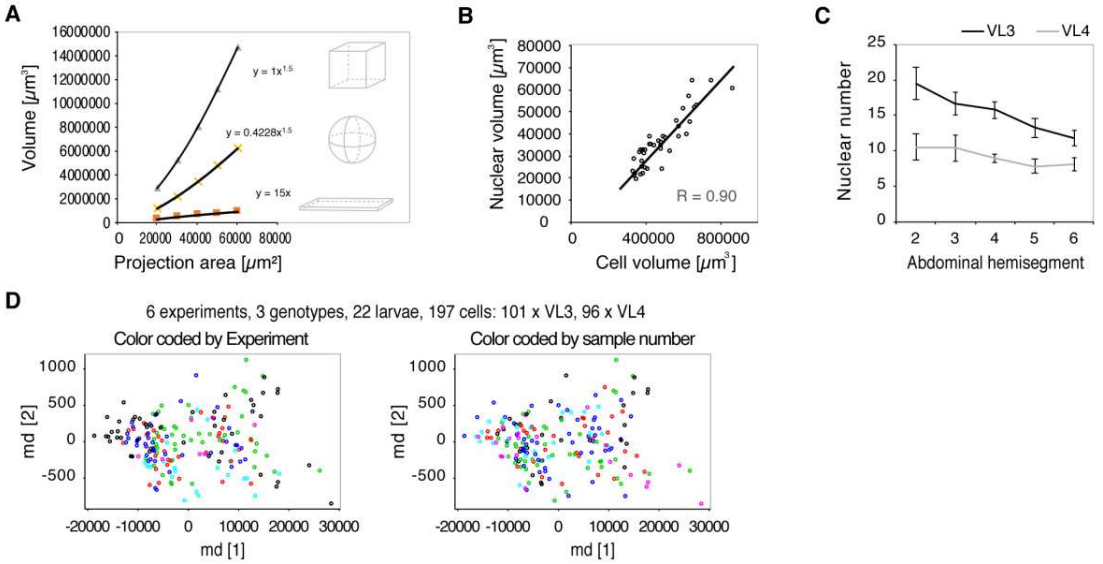

Figure S1. Quantification of VL cell and nuclear sizes. Related to Figure 1
(A) Relationships between volume and area measurements change with the shape of a 3D object. For flat VL muscles, increases in cell area correlate with only minor changes in cell volume compared to other cell shapes.
(B) Scatter plot of cumulative nuclear volume and VL cell volume, showing a similar global scaling relationship than quantification in 2D. n (cells) = 42, n (nuclei) = 572.
(C) Number of VL3 (black) and VL4 (gray) muscle nuclei plotted over the corresponding abdominal hemisegment positions along the larvae. Lines represent mean values. $n_{VL3} = 102$, $n_{VL4} = 97$.
(D) Unsupervised multidimensional cluster analysis of VL muscles from 3 different genetic control backgrounds (w^{1118}, *Dmef2-GAL4;UAS-2xEGFP*, *Dmef2-GAL4;UAS-GFP RNAi*, two experimental replicates each) using the following parameters: cell size, cell shape (aspect ratio), nuclear number, total nuclear area, axis level (abdominal hemisegment number). Cells cluster in 2 groups, which clearly correspond to the VL3 and VL4 muscles (Figure 1G) but show no bias for experimental replicate (left) or individual larvae (right). $n_{VL3} = 102$, $n_{VL4} = 97$.

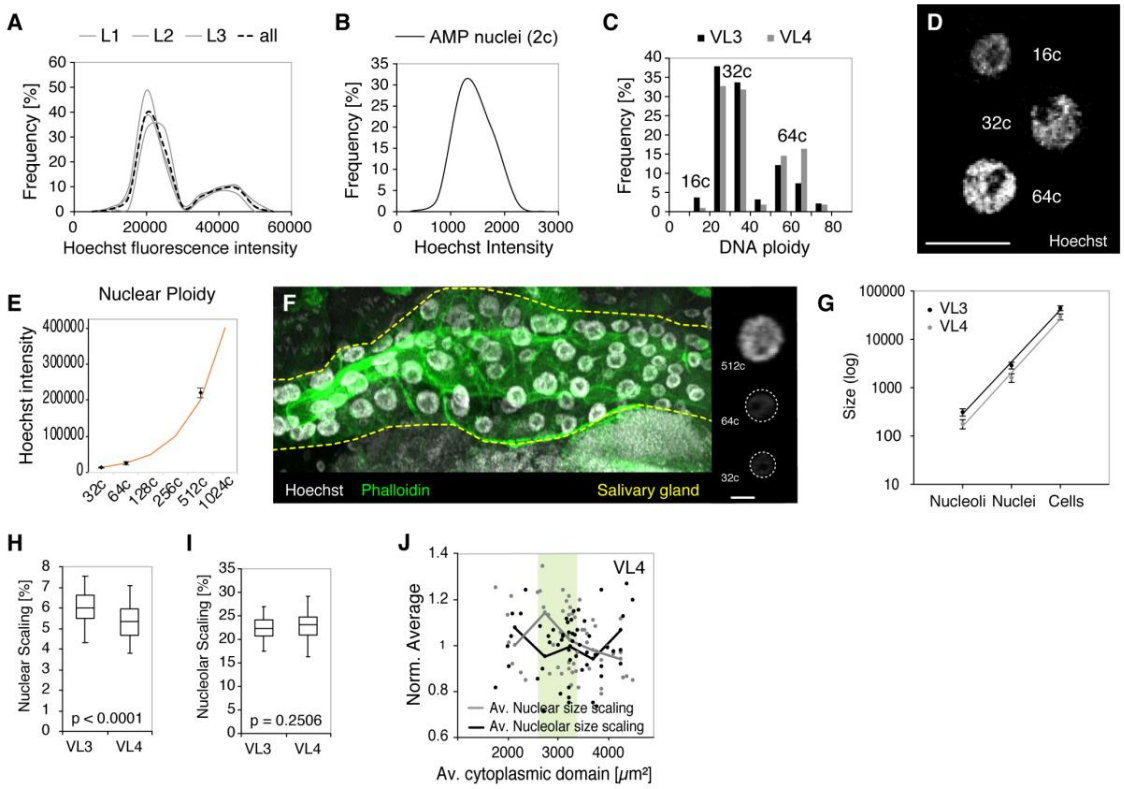

Figure S2. Muscle nuclei establish precise global scaling with cell size. Related to Figure 2.
(A) Histogram of DNA (Hoechst) fluorescence intensities in individual VL muscle nuclei from 3 individual larvae (L1-L3, gray). VL nuclei per larva n ≥ 100. Black dashed line represents mean values.
(B) Histogram of Hoechst intensities in diploid (2c) adult muscle progenitors (AMPs). n = 90.
(C) Histogram of calculated DNA copy numbers (ploidy) for nuclei plotted in (B). Peaks correspond to nuclei containing 16, 32 or 64 copies (c) of DNA.
(D) Example VL nuclei containing different amounts of DNA. Ploidy numbers are indicated.
(E, F) Comparison of DNA content in VL nuclei and other polyploid nuclei in the *Drosophila* larvae. Similar to previous publications (Frawley and Orr-Weaver, 2015), our method of calculating nuclear DNA content resulted in salivary gland nuclei (n=10) containing a minimum of 512c. Salivary gland and corresponding nuclei were labeled with phalloidin (green), and Hoechst (gray), respectively.
(G) Cumulative nucleolar and nuclear sizes scale linearly with cell size on a log scale.
(H, I) Boxplots comparing global nuclear scaling (H) (% nuclear area per cell) and global nucleolar scaling (I) (% nucleolar area per cell) in VL3 and VL4 muscles (n_{VL3}=54, n_{VL4}=54). Medians, 27/75 percentiles, min/max values. Both scaling parameters are significantly lower in VL4 muscles (p values indicate Student's t test result).
(J) Nuclear size scaling and nucleolar size scaling plotted against the average size of the cytoplasmic domains within VL4 cells (for VL3, see Figure 2K). Note: highest nuclear scaling values are associated with optimal cytoplasmic domain sizes (green area), while smaller or larger domain sizes correlate with increased nucleolar scaling and proportionally smaller nuclei. (n_{VL3}=54, n_{VL4}=54)
Scale bars, 50µm (D), 25µm (F).

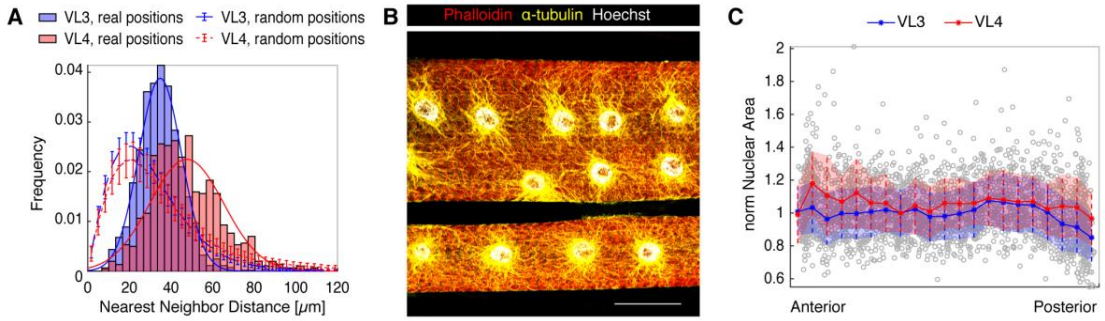

Figure S3. Nuclear positioning regulates individual nuclear sizes. Related to Figure 3.
(A) Histogram of Nearest Neighbor Distances (NNDs) in VL3 (blue) and VL4 muscles (red) in comparison to random distribution of nuclei (for simulation details see methods). NNDs follow normal distributions (blue and red lines) with mean +/- SD: 34.8 +/- 10.3 and 47.6 +/- 17.7 for VL3 and VL4 muscles, respectively.
(B) VL3 and VL4 muscles labeled with phalloidin (red) and anti-α-tubulin antibodies. Nuclear DNA (Hoechst) is shown in white. Scale bar: 50 μm.
(C) Distribution of normalized Simulated Nuclear Areas (Simulated Nuclear Area*No. of Nuclei/Cell Area) along the cell length (see Figure 3E and Mathematical Supplement for simulation details). Thick lines show averages, shaded regions correspond to standard deviation.

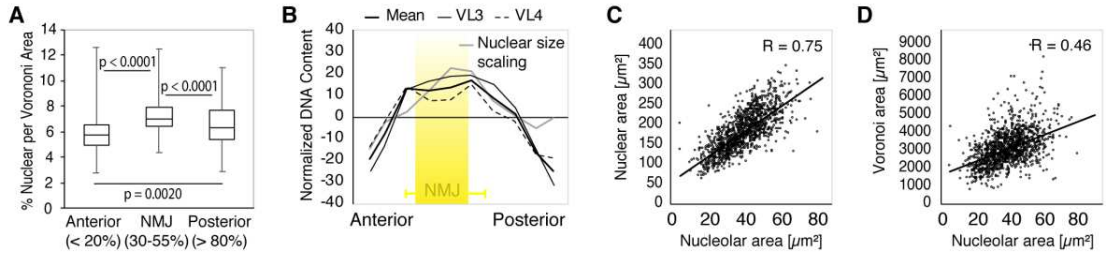

Figure S4. Local scaling of nuclear size, DNA content, and nucleolar size. Related to Figure 4.
(A) Box plot comparing median nuclear size scaling (% nuclear area per Voronoi domain) at the anterior and posterior MTJs (20% of cell length) and the NMJ (30-55% of cell length). p values determined by Student's t test.
(B) Normalized nuclear DNA content plotted against cell length. Mean values for VL3 and VL4 muscles are indicated. Gray line shows normalized nuclear size scaling for reference. NMJ region (yellow box) as in (Figure 4B).
(C,D) Scatter plots demonstrating local scaling of nucleolar areas with nuclear areas (D) (R=0.75) and with Voronoi domain areas (E) (R=0.46).
Sample numbers: n=950 nuclei (A), n=1286 nuclei (B-D)

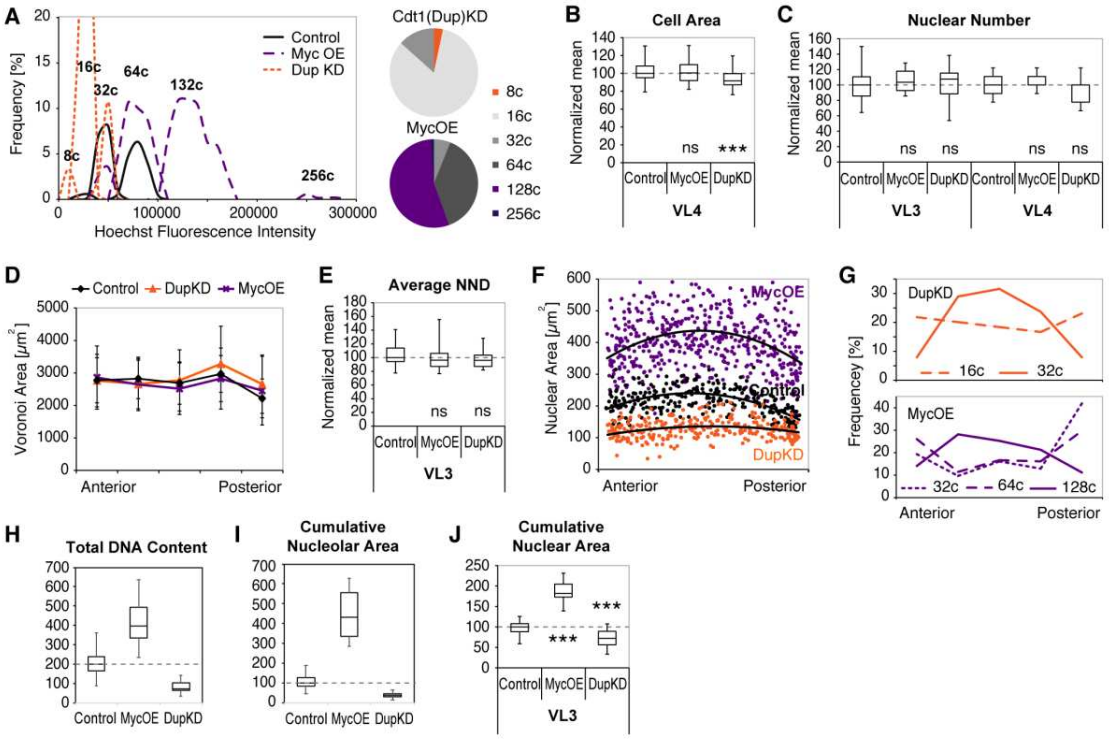

Figure S5. Muscle specific manipulations of nuclear DNA content. Related to Figure 5.
(A) Left: Histogram of DNA (Hoechst) fluorescence intensities showing decreased nuclear DNA content in Cdt1(Dup)KD (n_{VL3}=25, n_{VL4}=24) and DNA increased DNA content in Myc OE muscles (n_{VL3}=21, n_{VL4}=19). Right: Pie charts of nuclear ploidies in Cdt1(Dup)KD (n_{VL3}=25, n_{VL4}=24) and MycOE muscles. Ploidy classes not found in control muscles are highlighted in orange (8c; Cdt1(Dup)KD) and purple (128c, 256c; MycOE).
(B,C) Box plots (whisker, min/max values; boxes, 25/75 percentiles) comparing median cell areas(B) and nuclear numbers(C) in Cdt1(Dup)KD, Myc OE and control muscles (dashed line indicates median). Student's t test results: (B) MycOE, p= 0.1268, Cdt1(Dup)KD, p=0.1269, (C) MycOE: p_{VL3}=0.9959, p_{VL4}= 0.3720, Cdt1(Dup)KD: p_{VL3}=0.0268, p_{VL4}=0.0002.
(D) Voronoi domain areas along the long cell axis (mean +/- SD). Colored lines indicate genotype.
(E) Boxplot (whisker, min/max values; boxes, 25/75 percentiles) showing nearest neighbor distance (NND) in VL3 muscles of Cdt1(Dup)KD, Myc OE and control larvae. Student's t test results: p = 0.1638 (MycOE) and p = 0.5448 (Cdt1(Dup)KD).
(F) Scatter plots showing distribution of nuclear areas along the long cell axis.
(G) Histograms showing distribution of nuclear ploidies in Myc OE (**h**) and Cdt1(Dup)KD (**i**) muscles.
Sample numbers: Control, n_{VL3}=28, n_{VL4}=35 cells; Cdt1(Dup)KD, n_{VL3}=39, n_{VL4}=35 cells; MycOE, n_{VL3}=18,
(H-J) Boxplots (whisker, min/max values; boxes, 25/75 percentiles) showing median cumulative DNA content, nucleolar area and nuclear area in VL3 muscles of Cdt1(Dup)KD, Myc OE, and control larvae. Student's t test results are p < 0.0001 for both genotypes in (H-J)
Sample numbers: Control, n_{VL3}=28, n_{VL4}=35 cells; Cdt1(Dup)KD, n_{VL3}=39, n_{VL4}=35 cells; MycOE, n_{VL3}=18, n_{VL4}=19 cells

Mathematical Supplement for: Nuclear Scaling is coordinated among individual nuclei in multinucleated muscle fibers.

S. Windner, A. Manhart, A. Brown, A. Mogilner, M. Baylies

1 Space-sensing Model Details

Here, we provide details on the space-sensing model presented in the main text. In short, we suggest a mechanism which allows nuclei to sense the size of the space around them and adjust their size accordingly. The shape of larval muscle cells VL3 and VL4 is roughly a cuboid with typical dimensions

$$\text{width} \times \text{length} \times \text{depth} = 70\mu m \times 500\mu m \times 13\mu m,$$

i.e. the cells are very flat. Nuclei have the shape of flat cylinders, or discs, all positioned on one of the broad cuboids faces. We started by describing the 2D model, in which we neglect the cells' depths; the 3D variant of the model is described below. We hypothesized that a signal molecule, with concentration $s(x, y, t)$ at position (x, y) and time $t > 0$, is produced randomly anywhere in the cell with a constant rate γ. We also hypothesized that the signal molecules diffuse with diffusion constant D. If a molecule encounters a nucleus, it is taken up or absorbed by the nucleus. At each time instant, the nucleus adjusts its size, A according the total amount of signal it receives. The nuclear size, A, denotes the 2D area of the disc shaped nucleus, however since the nuclei are very flat and their depth was not observed to be variable, the nuclear area is proportional to its volume (see main Fig. 1).

To explore this model mathematically, we formulated the following system of differential equations:

$$\begin{aligned} \partial_t s = D\Delta s + \gamma \qquad & (x, y) \in \mathcal{C}, \qquad (1) \\ \nabla s \cdot n = 0 \qquad & (x, y) \in \partial\mathcal{C}, \\ s = 0 \qquad & (x, y) \in \bigcup_{i=1}^{N} \partial\mathcal{N}_i. \qquad (2) \end{aligned}$$

Here $\mathcal{C}$ denotes the 2D cell excluding the space occupied by the nuclei and $\partial\mathcal{C}$ is the outer boundary. The vector n is the outward unit normal along this boundary. The nuclei are indexed with $i = 1, \dots N$ and $\partial\mathcal{N}_i$ is the boundary of the i-th nucleus. The first

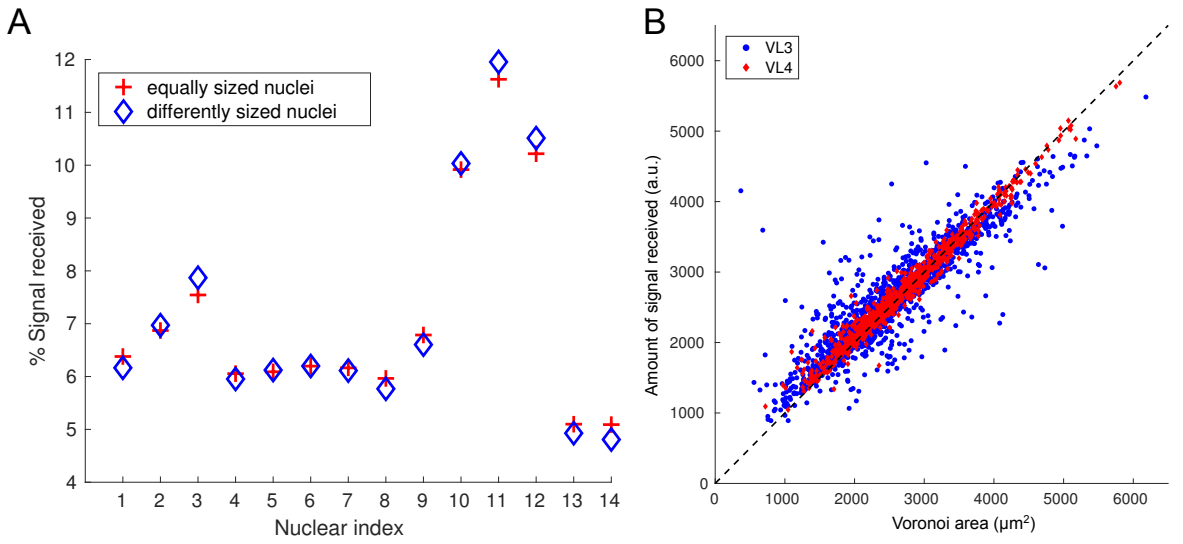

Figure M1: *A: For the example cell shown in Fig. M2, we compared the % of the total amount of absorbed signal received by each nucleus if we solve* (5) *for equally sized nuclei* ($45\mu m^2$)*, or having different sizes (using the measured nuclear areas). As can be seen, the difference is less than 0.5%. B: Comparing the geometrically determined Voronoi areas with the amount of signal received, calculated by using* (5) *and* (3).

and second terms in the right hand side of the first equation describe the signal molecule diffusion and activation (or synthesis) with rate γ, respectively. The second equation is the no flux boundary condition at the cell boundaries, and the third equation is the absorption boundary condition at the circular nuclear boundaries.

The amount of signal the i-th nucleus receives per unit time is given by the curve integral:

$$S_i = -D \int_{\partial \mathcal{N}_i} \nabla s \cdot n \, \mathrm{d}\Gamma_i, \tag{3}$$

where n is the unit normal pointing from the cell towards the nucleus. For the area of the i-th nucleus, A_i, we assume that:

$$\dot{A}_i = aS_i + b\,(A_{\min} - A_i). \tag{4}$$

The first term on the right-hand-side describes the growth of the nuclear area proportional to the amount of the signal, S_i, received per unit time. The second term is based on the assumption that, in the absence of any signal, the size of the nucleus approaches the minimal size, $A_{\min}$.

The steady state approximation. If we assume that the signal dynamics take place on a time scale faster than that of the nuclear growth, which is reasonable, then we can at each time step approximate (1) by its steady state solution:

$$0 = D\Delta s + \gamma \qquad (x, y) \in \mathcal{C}, \tag{5}$$

and iterate between solving this steady state equation and updating the nuclear sizes according to (4). After such simulations, we observed that the amount of signal each nucleus received, S_i, depended only very mildly on its size – and thereby time – but rather depended almost exclusively on its fixed position (see Fig. M1A). This observation justifies the following procedure to determine the nuclear equilibrium sizes: 1. Set a fixed initial nuclear area for all nuclei and solve (5) with this geometry to obtain the signal concentration $s(x, y)$. 2. Calculate the amount of signal each nucleus receives S_i per unit time using (3). 3. Calculate the equilibrium nuclear areas as the steady state solutions to (4), i.e.

$$A_i = A_{\min} + \frac{a}{b} S_i.$$

To obtain the minimal nuclear area $A_{\min}$ and the signal sensitivity $\alpha = a/b$, we solved the associated least-squares problem of the overdetermined system, i.e. we determined $A_{\min}$ and α so that the error between the measured and predicted nuclear areas in the Euclidean norm becomes minimal. This yielded $A_{\min} = 83\mu m^2$ and $\alpha = 0.044\mu m^2$ per unit signal. The average relative error between the predicted and actual nuclear area was 16.9%.

Note that setting $D = \gamma = 1$ does not affect the result, and so we used these parameters and methods to obtain the results shown in all modeling figures in the main text. For the simulations, we used the Finite Element Method with quadratic elements and the adaptive mesh solver provided by Matlab's PDE Toolbox. We used the actual measured cellular outlines, positions and number of nuclei for 200 wild-type cells.

Results and interpretation. In our space-sensing model, the total amount of the signal produced (and hence also absorbed) per unit time is proportional to the total cell area. Since we assumed a linear dependence of the nuclear area on the amount of the signal received, the total predicted nuclear area increases linearly with cell area, as reported in the main text, Fig. 2G. However, our model goes beyond this cell-wide regulation of the nuclear area, since it suggests a mechanism for a local regulation of nuclear areas within each cell. This local regulation was evident in the experimental data if we normalized both nuclear areas and Voronoi areas by their per-cell-averages. We found that the local differences in the nuclear areas correlated with local differences in the Voronoi areas ($R = 0.45$, $p < 0.0001$). The amount of signal received by each nucleus, according to our model, was highly correlated with the size of its Voronoi domain (Fig. M1B, $R = 0.93$, $p < 0.0001$). Our model thereby offers a mechanistic explanation for both the cell-wide and some of the within-cell variation of the observed nuclear sizes. However, our space-sensing model does not explain why we see such a large dependence of nuclear size on nuclear distance to the cell poles (main text Fig. 3G). Reasons could lie in differences in signal production and/or signal transport near the poles.

Space-sensing for modified endoreplication. In the main text we discussed the effect of manipulating a muscle cell's ability to increase its DNA copy number through endoreplication. In particular we looked at mutants where endoreplication was reduced

through a knock-down (KD) of Ctd(Dup), and mutants where endoreplication was increased through overexpression (OE) of Myc. In the following we refer to them as KD and OE cells. We used our space-sensing model to determine the minimal nuclear area $A_{\min}$ and the signal sensitivity α for KD and OE cells and found the following changes compared to the wild-type:

- For OE cells both $A_{\min}$ and the sensitivity α roughly doubled ($A_{\min}$ increased by 106%, α increased by 87%).
- For KD cells $A_{\min}$ decreased by 11%, whereas α stayed roughly the same ($< 1\%$ increase).

The differences in $A_{\min}$ might reflect the changes in (minimal) space requirements for more/less DNA copy numbers, whereas the increased sensitivity for OE cells could mean that OE nuclei react more sensitively to received signals compared to wild-type cells.

2 Variants of the Space-Sensing Model

Several variants of the space-sensing model presented above are possible. As already discussed, solving the fully time-dependent problem has a negligible effect on the final result.

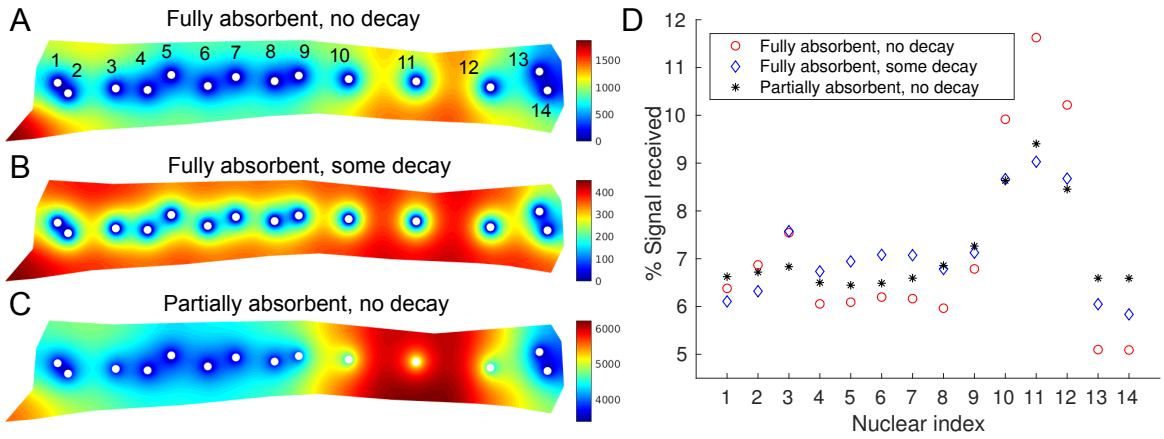

Figure M2: *A-C: Equilibrium signal distribution for three variants of the space-sensing model as described in the text. All three models use $D = \gamma = 1$. For A we used the basic model (fully absorbent, no decay). For B, we used $\delta = 0.002$, for C we used $\sigma = 0.03$. Note that the colorbars differ between A-C. D: Shown is the % of the total amount of absorbed signal received by each nucleus for the example cell and the models shown in A-C.*

Signal decay. As noted above, the amount of signal received according to the above model corresponded very well to the Voronoi areas of the nuclei. In the main text, Fig. 3F shows that the correlation between the nuclear areas and the Voronoi areas becomes sublinear for large Voronoi areas, i.e. the nuclei that are far away from their neighbors

are slightly smaller than the great size of their Voronoi areas would suggest. We tested mathematically if this could be due to a slow spontaneous decay of the molecular signal. Since, for large Voronoi areas, the signal takes longer to reach the nucleus, a greater part of the signal would decay before reaching the nucleus, compared to smaller Voronoi areas, which could explain the observed sublinearity. Mathematically, this means replacing (1) by

$$\partial_t s = D\Delta s + \gamma - \delta s \qquad (x, y) \in \mathcal{C},$$

where we assume a decay rate δ with units of per time. We tested different values of parameter δ and found that the average relative error stayed above 16%, i.e. we could not get a significantly better prediction of the nuclear size. However, when looking at the nuclei having the largest 2% of Voronoi areas in our sample, the average relative error between simulated and measured nuclear area dropped from 30.5% to 25.0% for a moderate amount of signal decay ($\delta = 0.0005$), as expected.

If the value of δ is chosen to be too large, the prediction becomes worse, since all nuclei receive roughly the same amount of signal, independent of the space around them. Fig. M2A,C shows that away from the nuclei, the signal distribution is more even, when there is the assumed decay. Fig. M2D compares how the percentage of obtained signal varies for the two cases. As expected, signal decay leads to less variation in the signal per nucleus within a cell.

Finite nuclear signal uptake speed. In the model described above, we assumed that all of the signal molecules that reach a nucleus are immediately taken up or absorbed. However, it is also reasonable to assume that there is a finite absorption rate σ. This would change the boundary condition (2) to

$$D\nabla s \cdot n = \sigma s \qquad (x, y) \in \bigcup_{i=1}^{N} \partial\mathcal{N}_i.$$

The original model can be seen as limiting case for $\sigma \to \infty$. We performed tests with different values of σ and found that as long as σ is large enough, the general result was hardly affected. We were not able to obtain significantly better fits between the calculated and the measured nuclear area by varying σ. Fig. M2A,C shows the different signal distribution for an example cell using finite and infinite nuclear signal uptake speed and Fig. M2D compares how the percentage of obtained signal varies for the two cases. As can be observed, finite signal changes the overall signal distribution and also leads to less variation in the signal per nucleus within a cell.

Space-sensing in 3D. Next, we explored how solving in three space-dimensions affects the solution. Since nuclei are positioned on one surface of the muscle cell, we can model them in the 3D setting by changing the boundary condition on that face from impenetrable (Neumann boundary condition) to fully absorbent (Dirichlet boundary condition) wherever

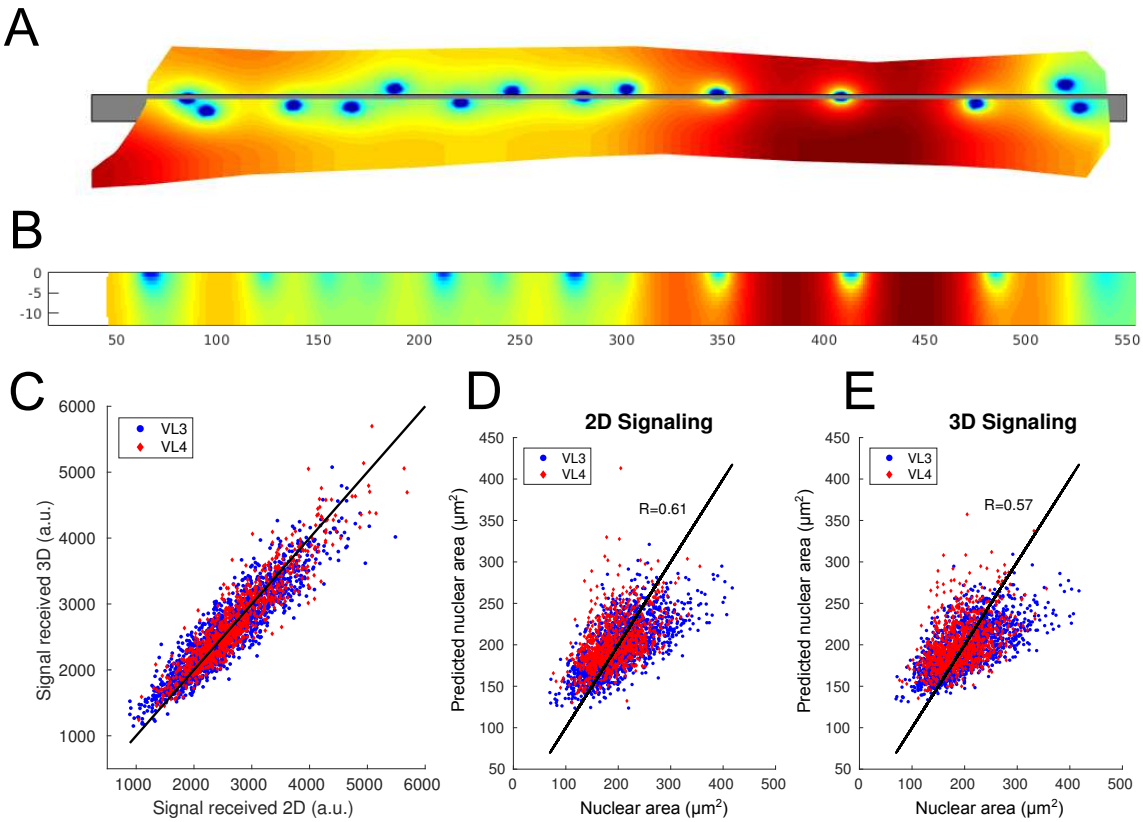

Figure M3: *A: Signal distribution on the surface of a 3D cell as described in the text. Blue = low concentration, red = high concentration. B: Slice through the cell along the plane shown in A. C: Comparing the amount of signal received for 2477 nuclei between the 2D and the 3D model. D-E: Predicted vs measured nuclear areas of the 2D and 3D model.*

there is a nucleus. Mathematically this means solving the following system of equations:

$$\begin{aligned} 0 &= D\Delta s + \gamma \qquad (x,y,z) \in \mathcal{C}, \\ \nabla s \cdot n &= 0 \qquad (x,y,z) \in \partial\mathcal{C} \cap \bigcup_{i=1}^{N} \mathcal{N}_i, \\ s &= 0 \qquad (x,y,z) \in \bigcup_{i=1}^{N} \mathcal{N}_i, \end{aligned} \tag{6}$$

where now $\mathcal{N}_i$ are *filled* 2D discs, representing the nuclei. Figures M3A and B show the signal distribution on the surface of the cell and along a cut through the cell, respectively. As expected, signal amounts are low near the nuclear discs. Upon comparing the amounts of signal per nucleus between the 2D and 3D simulation in Fig. M3C, we see that they are very similar. Using the amount of signal received according to the 3D simulation still allows predicting the measured nuclear area very well, however, slightly less well than using the 2D simulation. A speculative explanation could be that due to the sarcomeric structures in the cell, the diffusing signal cannot actually access the full depth of the cell.

3 Future Space-sensing Models

Active signal transport. So far the signal movement described was purely passive. However, it is possible that the signal is being transported actively, e.g. along microtubule tracks towards the nuclei or through the cell. This could be included in our model in a straight-forward manner.

Space-sensing in mammalian muscle cells. The geometry of mammalian skeletal muscles differs significantly from those of the fruit fly cells that we studied. Mammalian skeletal muscle cells form long, thin cylinders which contain myofibrils, within which the force-generating sarcomers are located. Muscle nuclei are positioned near the outer surface of the cylinder. Previous work [1] suggests that the position of the nuclei is consistent with a repulsion model similar to that presented in the main text. Our space-sensing model could be easily adapted to mammalian muscles, when data on correlations between nuclear sizes and spacing in such muscles become available. The different geometry could lead to different scaling laws: For example the signaling molecule could be diffusing in the full 3D cylinder or merely close to its 2D surface. Additionally, signal uptake could cause a linear increase in either nuclear volume or surface area, and finally also signal leakage from the nuclei could affect potential scaling laws.

References

[1] Bruusgaard J, Liestøl K, Ekmark M, Kollstad K, Gundersen K. Number and spatial distribution of nuclei in the muscle fibres of normal mice studied in vivo. J of Physiol. 2003;551(2):467–478.